



TECHNICAL ARTICLE

Screw Extrusion Additive Manufacturing of Carbon Fiber Reinforced PA6 Tools

G. Barera , S. Dul, and A. Pegoretti

Submitted: 25 July 2022 / Revised: 12 April 2023 / Accepted: 15 April 2023 / Published online: 2 May 2023

The creation of tools by additive manufacturing is becoming increasingly convenient for CFRP one-off and small batch production. Screw extrusion additive manufacturing of thermoplastic polymers has boosted the development of large format manufacturing solutions. Interlayer adhesion and anisotropic properties of a 3D printed part are indisputably key aspects of tool manufacturing process. In this study, thermal and mechanical properties of large format 40% carbon fiber reinforced polyamide 6 3D printed tools were determined. Moreover, the influence on part performance of two main printing parameters, deposition temperature and extruding pressure, was analyzed with respect to polymer melt rheology. The printed material revealed a highly anisotropic thermal and mechanical behavior associated with the alignment of the high carbon fiber content. The optimal process window was identified in terms of substrate deposition temperature. Along the print direction, no major impact on tensile and flexural mechanical properties was detected, while the injection molding values were exceeded by approximately 10%. The layer adhesion was estimated by measuring the stress at break on transversely Z-oriented specimens. Higher deposition temperatures and pressures, combined with lower viscosity, promote wetting and bond formation between layers, ultimately leading to more consistent performances. The best results in the transverse direction were achieved between 140 and 160 °C, reaching roughly a fifth of the longitudinal values. A significant drop in performance was detected below 120 °C, which was identified as the minimum process temperature. A post-process annealing heat treatment was also investigated, no beneficial outcomes were reported.

Keywords large format additive manufacturing, layer adhesion, mechanical properties, polyamide 6, screw extrusion, tool 3D printing

Abbreviations

ABS	Acrylonitrile butadiene styrene
AM	Additive manufacturing
CTE	Coefficient of thermal expansion
DMTA	Dynamic mechanical thermal analysis
DSC	Differential scanning calorimetry
FFF	Filament fused fabrication
FRP	Fiber reinforced polymer
LFAM	Large format additive manufacturing
LFA	Laser flash analysis
MFR	Melt flow rate
PA6	Polyamide 6
PC	Polycarbonate
PEI	Polyether imide
PESU	Polyether sulfone
SEAM	Screw extrusion additive manufacturing

1. Introduction

Additive manufacturing (Ref 1) of thermoplastic polymers, commonly known as 3D printing, is a rapidly growing technology in the industry and consists of building a part by depositing molten material layer by layer. A 3D model is sliced with a determined layer height by a software, also known as slicer, generating the deposition path for each layer. Additive manufacturing is a process unique in terms of flexibility; the possibility to produce complex net shapes within a short time frame and minimize material waste makes it an attractive technology for rapid prototyping, design, and small batch production (Ref 2). In the last few years, large format additive

manufacturing (LFAM) 3D printers based on screw extrusion technology have been developed and released (Ref 3-5). Compared to fused filament fabrication (FFF), screw extrusion 3D printing machines are capable of processing reinforced polymers up to 60% of fiber content using pellets as feedstock material and, thanks to the high mass flow, produce parts of several meters in length (Ref 6). This technological achievement has paved the way for the production of equipment and tooling for parts in structural composite materials, like assem-

G. Barera, Department of Industrial Engineering, University of Trento, Via Sommarive 9, 38123 Trento, Italy; and CMS S.p.A., Via A. Locatelli 123, 24019 Zogno, BG, Italy; **S. Dul**, Empa, Swiss Federal Laboratories for Materials Science and Technology, Lerchenfeldstrasse 5, 9014 St. Gallen, Switzerland; and **A. Pegoretti**, Department of Industrial Engineering, University of Trento, Via Sommarive 9, 38123 Trento, Italy. Contact e-mail: giacomo.barera@unitn.it.

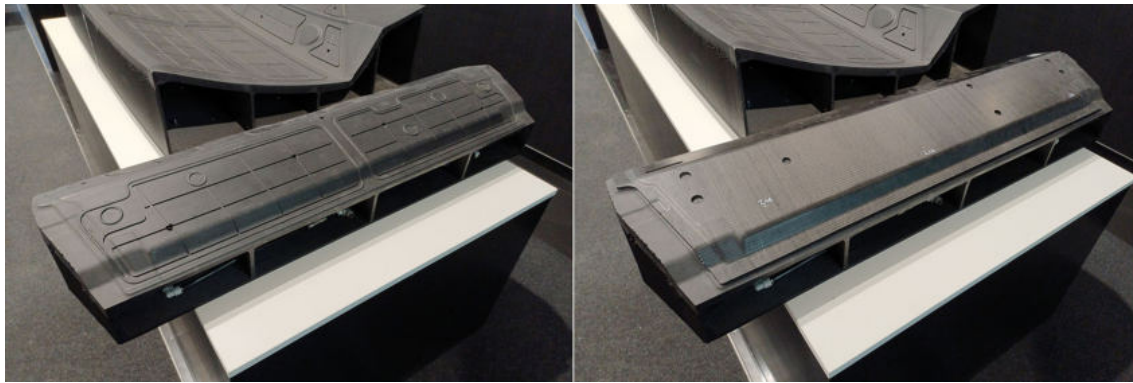


Fig. 1 Example of a machining vacuum fixture for carbon fiber composite parts. The tool is 1200 × 400 × 300 mm and was printed with carbon fiber reinforced PA6

bling calipers, molds, and jigs, at a fraction of the time and cost of currently used technologies (Ref 7, 8).

Different tooling applications ask for different material properties and target prices. In most cases, short carbon or glass fiber filled polymers are used; typical fiber content ranges between 15 and 40%. Reinforcement is effectively used to enhance mechanical properties, dimensional stability at service temperature, and abrasion resistance (Ref 9-11).

In the framework of large format 3D printed tooling manufacturing, carbon fiber reinforced acrylonitrile butadiene styrene (ABS) copolymer (Ref 12) and nylon (Fig. 1) are typically used for room temperature applications like low-temperature curing prepreg master, trim fixture, and drill jig. Carbon fiber reinforced polycarbonate (PC) can be used up to 130 °C in applications such as autoclave and thermoforming molds, preforms, and infusion tools (Ref 13). For higher temperature applications, like direct autoclave mold, carbon fiber reinforced polyether imide (PEI) and polyether sulfone (PESU) are normally employed with continuous service temperatures close to 180 °C (Ref 14, 15).

Nevertheless, as a result of the intrinsic directionality of the deposition and the layer-by-layer approach, 3D printing is a thermally uneven process that produces highly anisotropic parts (Ref 16, 17). Indeed, the polymer melt, by flowing through the terminal cylindrical portion of the nozzle, realigns the polymer chains and fibers in the print direction inside the material beads.

Large 3D printed parts, which are more prone to temperature unevenness, are likely to be affected by warpage and faulty adhesion between layers, reducing the part machinability and the final tool quality. Layer adhesion is the most significant aspect affecting the performances of additively manufactured products. Poor adhesion between the layers may cause material separation, thus resulting in part failure. Cracks and fractures mainly develop during machining when the material is removed and undergoes severe localized stresses (Fig. 2) (Ref 18).

Additively manufactured products are, by their very nature, characterized by anisotropic mechanical properties (Ref 19). Along the print direction (X), the mechanical properties are mostly determined by the orientation of both polymer chains and fibers induced by the strand deposition. On the other hand, along the build direction (Z), the strength of the material is limited by the degree of bonding between the printed layers (Ref 20). In fact, by defining the ultimate tensile strength of a bulk material as σ_0 , the fracture strength between layers is equal to $D \cdot \sigma_0$, where D is the degree of interfacial weld healing and ranges between zero and one.



Fig. 2 Carbon fiber reinforced polyamide 6 trimming tool showing an interlayer crack growth developed during machining

Bond formation is a temperature-driven phenomenon strictly related to polymer diffusion through the interfacial contact area between layers. Surface wetting is the first stage of bond formation and is promoted by the lower viscosity of the melt. The deposited molten polymer reheats the surface of the layer below to the adhesion temperature inducing neck growth. The interfacial contact area acts as a gap-bridging site in which random diffusion of polymer chains can take place. During the printing process, the material undergoes heat loss by thermal conduction with the underlying layer as well as environmental convection and radiation. Cooling leads to a rapid increase in viscosity and, therefore, diffusion at the layer interface is suddenly inhibited together with bond formation, which instead benefits from longer diffusion time at higher temperatures (Ref 15, 17).

Since the 70 s, two models have been proposed to estimate the rate of diffusion of polymeric materials as a function of their thermal history (Ref 21, 22). Based on these theories, Bartolai has recently developed a method for predicting the degree of healing by considering the average reptation time of an amorphous polymer, T_{REP} (Ref 23). This parameter can be derived from the time-temperature superposition master curve of the shear storage and shear loss moduli of the polymer G' and G'' experimentally obtained using a plate-plate rheometer

and by repeating the measurement over a wide range of temperatures and frequencies. To estimate the healing degree at the bond interface and overall bond strength, the reptation time has to be compared to the welding time obtained from the interface thermal history during cooling.

A different approach was proposed by Yardimci, who defined the bonding potential, as an indicator that summarily estimates the degree of adhesion by measuring the time that the material spends above a specific critical temperature T_{CR} (Ref 24). For a given material, the critical temperature is defined as the temperature below which no further adhesion develops between the two layers. The simplicity of calculation makes this method a suitable option for most technological and industrial applications.

For amorphous polymers, the critical temperature can be related to the glass transition temperature above which mobility of the polymer chains occurred (Ref 25). In the case of semicrystalline polymers, the crystallization dynamic has to be taken into account. Bond and crystalline structure formation occur concurrently, limiting molecular diffusion at the interface and reducing the adhesion between layers resulting in lower mechanical properties. For adequate molecular diffusion, the critical adhesion temperature of the interface is set equal to the polymer melting temperature. The longer the material is held above its critical temperature, the better the layer adhesion (Ref 26-29).

From a process standpoint, interlayer bond formation is promoted by increasing temperature and reducing the cooling rate of the interface. Higher extrusion temperature, bigger strands with lower W/H aspect ratio, limited cooling, and shorter layer time should theoretically produce better interlayer adhesion. The molten polymer needs to come into full intimate contact with the underlying layer in the fastest way possible; wetting is improved by higher extrusion pressures and, in the case of shear-thinning polymer melt, higher shear rates produced with an optimized nozzle geometry and appropriate print parameters (Ref 29, 30).

In addition to the clear benefits provided by carbon fiber reinforced polymer, a high filler content also works against layer adhesion. Fibers significantly increase viscosity and impede the motion of polymer chains hindering diffusive dynamics at the interface; moreover, they reduce matrix content, the prime driver of bond formation (Ref 29, 31). In the extreme scenario of a severely poor fiber–matrix interface, it might act as an intralayer structural discontinuity (Ref 32). It must further be mentioned that a high carbon fiber percentage also leads to a major increase in polymer thermal conductivity promoting strand cooldown. According to laser flash analysis (LFA) measurement, the thermal conductivity of a neat nylon ranges between 0.24 and 0.28 W/m°C, a fraction of the one measured for the carbon fiber reinforced PA6 under investigation which resulted in 0.5 and 2.3 W/m°C, respectively, in transversal (Z) and print (X) direction.

A tool, however, does not serve any structurally demanding purpose and, in most applications, does not undergo any significant loading beyond thermal and self-weight induced stresses; the required mechanical properties are mostly related to handling and machining.

Nevertheless, in tool production, the presence of porosity, void, and cracks compromises the required vacuum integrity and/or the surface finish of the final part. Thermal stability, predictable expansion, low residual stresses, and minimum warpage are also crucial for mold applications. Such quality criteria can only be met with a correct printing strategy and

proper adhesion between layers by processing the material in the optimal process window with the appropriate parameters.

During extrusion, the strand width to nozzle diameter ratio governs the fiber alignment within the deposited strand. Assuming a fixed nozzle geometry, wider beads are typically associated with a lower degree of fiber alignment since the polymer melt, exiting the nozzle, has to spread out of the print direction more than smaller strands. Fiber orientation affects part performance and thermal stability by constraining the matrix thermal expansion along the printing direction. During cooling and solidification of the polymer, shrinkage results in internal stresses and part warpage. For semicrystalline polymers, contraction is intensified by the phase transition. As stresses build up, poor adhesion layers may fail during printing, and stress relaxation caused by material removal in machining can deform it. A heavily aligned fiber restricts polymer matrix shrinkage and expansion along the print direction and enables dimensional control and tailoring of the printed part (Ref 15, 17, 33, 34).

For this study, a 40% carbon fiber reinforced polyamide was selected. Thanks to the fiber content, the material has great mechanical properties at room temperature and good thermal stability up to 50 °C. Mass and cost saving make it a competitive replacement for traditional technologies used for machining jigs, assembling tools, and low-temperature resin lamination mold and master.

This research aims at defining the optimal process window to deliver a printed part that satisfies the quality level of industrial tool manufacturing. The influence of the main printing parameters affecting the processing of a carbon fiber reinforced PA6 by screw extrusion additive manufacturing is examined. The impact of deposition temperature, extruding pressure, and shear viscosity interlayer degree of bonding is analyzed. Layer adhesion and part performance are evaluated in terms of longitudinal and transversal elastic modulus and stress at break. The sample strand morphology and fracture surface are investigated as well. Ultimately, a post-print heat treatment to improve adhesion between layers is considered.

2. Material and Methods

2.1 Material

In this study, a 40% carbon fiber reinforced polyamide 6 (AKROMID® B3 ICF 40) produced by Akro-plastic GmbH (Niederzissen, Germany) was used. The material, designed for the injection molding process, has a 40% of recycled content (Ref 35). Thermogravimetric analysis performed between 30 and 700 °C under nitrogen atmosphere with a Mettler TG50 thermobalance (Columbus, Ohio, US) revealed a 37% mass residue.

According to the manufacturer's specification, an injection-molded sample in the dry-as-molded condition should achieve an elastic modulus of 30 GPa with a tensile strength of up to 220 MPa. A flexural modulus of 25 GPa and flexural strength are declared in the technical data sheet (Fig. 3).

Such mechanical performance can be met thanks to the high carbon fiber content that makes the material extremely rigid up to 50 °C. As reported in the dynamic mechanical thermal analysis curves in Fig. 4, the glass transition temperature by storage modulus onset of X samples is located at 55.5 while at 49.1 °C for Z ones. At this temperature range, which is fifteen degrees below the glass transition temperature measured by

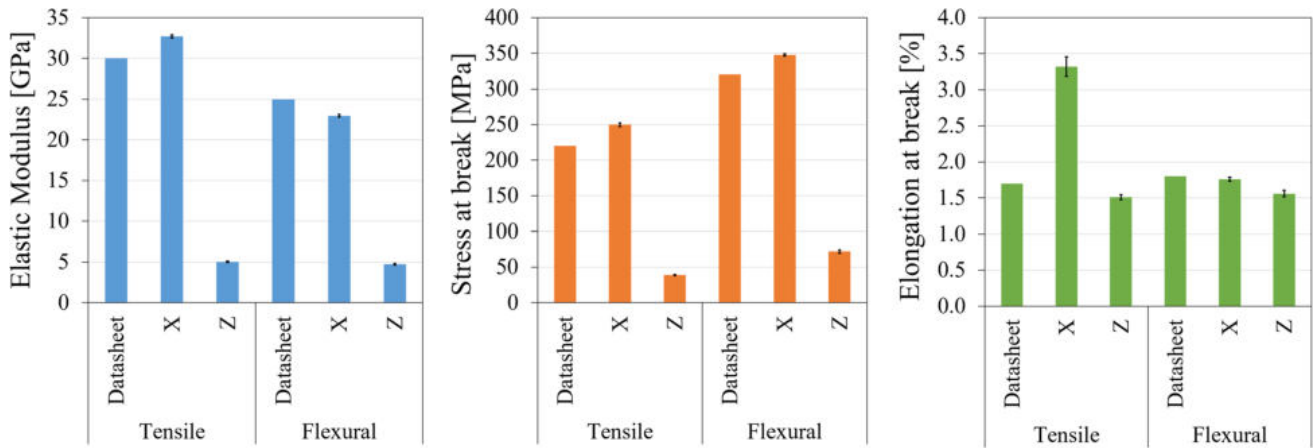


Fig. 3 Longitudinal (X) and transversal (Z) tensile mechanical properties of fully machined samples printed at optimal deposition temperature

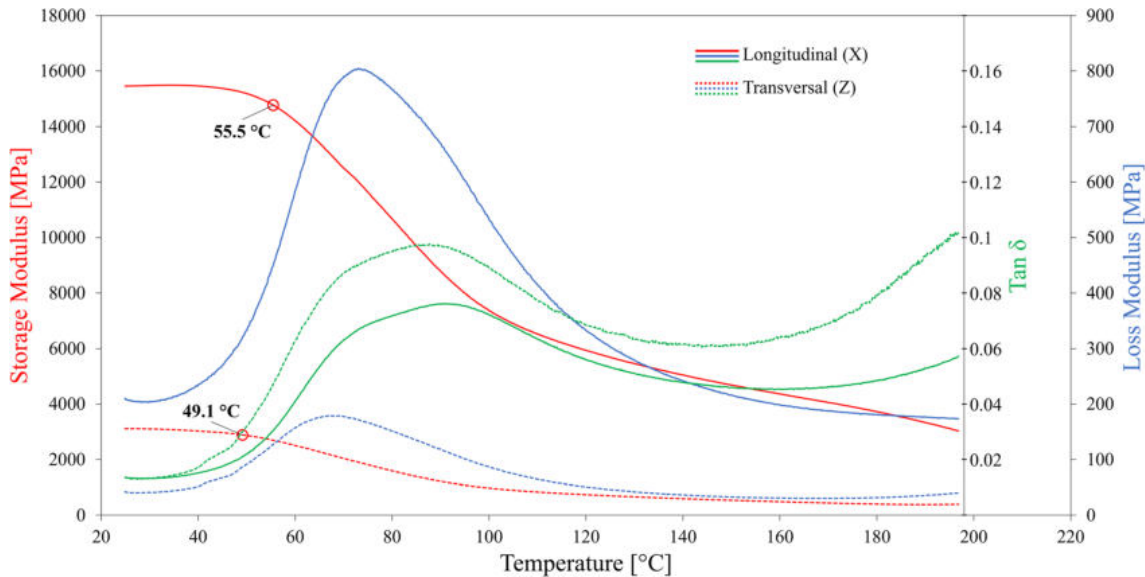


Fig. 4 Dual-cantilever mode dynamic mechanical thermal analysis (DMTA) curves of 40% carbon fiber reinforced PA6 longitudinal (solid) and transversal (dashed) 3D printed samples. Storage and loss moduli, and $\tan \delta$ are reported as function of temperature between 25 and 200 °C

DSC, the material also exhibits excellent thermal stability. By dilatometry analysis, the coefficients of thermal expansion (CTE) in X and Z directions were estimated, respectively, equal to 3.2 and 70 $\mu\text{m}/\text{m}^\circ\text{C}$ as shown by the strain–temperature curves in Fig. 5. Approaching the glass transition temperature at 67 °C, the curves, especially in the Z direction, show a rapid increase in thermal expansion, which can affect high-temperature material applications. X and Z coefficients of thermal expansions differ by more than an order of magnitude. Such highly anisotropic behavior stems from the carbon fiber orientation within the strand. As the polymer goes through the cylindrical channel of the nozzle, the fibers align with the material flow along the print direction. Oriented carbon fibers enhance the mechanical properties in X direction and limit the thermal expansion and shrinkage of the polymer matrix resulting in a significant reduction of part distortion during printing (Ref 36).

Duty developed a print distortion criterion based on the maximum structure aspect ratio, defined as the ratio between part length and layer height, and the distortion ratio, the ratio

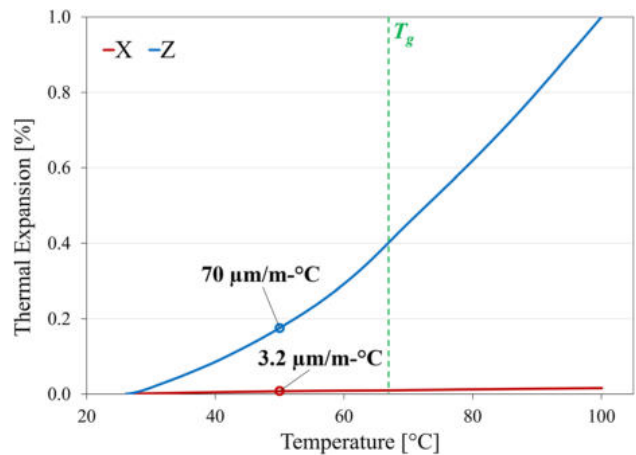


Fig. 5 Thermal expansion curve of X and Z oriented 40% carbon fiber reinforced PA6 3D printed sample measured by dilatometry from room temperature up to 100 °C

between part warpage and layer height. The distortion ratio, measured during cooling from crystallization temperature, must be less than one to avoid collision with the deformed underlying deposited structure (Ref 32). Based on the material coefficient of thermal expansion and considering a layer height of 1 mm, it would not be possible to print parts larger than 140 mm without securing the part on the build plate. Although it may not seem much, similar materials for low-temperature applications, such as neat and 20% carbon fiber reinforced ABS, exhibit lower values of 38 and 87 cm, respectively. Anisotropic CTE values, especially along the build direction, must be taken into account for print arrangement and dimensional compensation when tight tolerances tools are requested.

Moreover, the material ensures excellent surface finish and abrasion resistance. Low surface roughness, associated with no surficial defects, decreases the chance of localized stress buildup that may lead to crack initiation and spread over the tool's service life. On a finished machined surface, average roughness R_a of 0.4 μm was measured using a MarSurf PS1 roughness tester (Mahr GmbH, Goettingen, Germany). Such quality was achieved by means of a $\text{\O}20$ mm two-flute carbide ball nose end mill spin at 9000 rpm, 0.2 mm step at 5000 mm/min as feeding rate. The surface hardness of the printed material is good as well; a hardness in the ranges 87-88 Shore D was recorded employing a Shore D Tester by Hildebrand GmbH (Wendlingen, Germany) equipped with a 4 kg weight according to ISO 868 (Ref 37).

Such features suit well room temperature tools manufacturing for which high dimensional stability, rigidity, abrasion resistance, and excellent surface finish are required; the primary applications are low-temp FRP lamination molds, vacuum fixtures, machining and trimming jigs, and assembly calipers.

According to the technical datasheet, the density of the pellets was found equal to 1.31 g/cm^3 , while the density of the printed sample ranges between 1.29 and 1.32 g/cm^3 (Ref 38).

Prior to using the material was dried at 110 $^\circ\text{C}$ for 6 h inside a 42 L FASTI KOCH ERD Xpert + dryer produced by Werner Koch Maschinentechnik GmbH (Ispringen, Germany).

2.2 Processing

2.2.1 3D Printing Setup. The present study is part of an ongoing project of the company CMS Spa (Zogno, Italy) focused on the development of an additive manufacturing solution for thermoplastic polymers; CMS Kreator Ares is a hybrid large format screw extrusion additive manufacturing (SEAM) system. The machine has a build volume of 1800 \times 2000 \times 800 mm and is suitable to process glass and carbon fiber reinforced thermoplastic polymers in granulated form with a maximum mass flow of 10 kg/h and a printing speed of up to 16,000 mm/min. The extruder unit is based on a $\text{\O}20$ mm single screw having a relatively low length/diameter ratio of 20:1 to reduce the overall dimensions. The extruder is equipped with five different heating zones; going from T_1 close to the material inlet to T_4 at the screw tip while T_5 is placed at the nozzle where a pressure probe and a thermocouple are also located to record the extrusion parameters of the melt. The machine spindle drives the extruder through a reduction gearbox. The extrusion unit can be automatically detached from the machining head and placed in a dedicated holding

station. Due to its hybrid feature, the machine can print and mill in situ a slightly over-dimensioned component to obtain the final finished tool.

The printing strategies commonly applied in large format tool manufacturing consist of an outer multi-shell box with few internal ribs as stiffeners (Fig. 1).

A 3D printed part is produced by depositing a layer of material in the molten state above a previously deposited layer up to the point where the final height and geometry are reached. Ideally, when a new layer is deposited it cools down from the extrusion temperature to the stage where it is rigid enough to withstand the weight of the following layer. Given a certain material, the cooling time is governed by the print strategy and the part geometry. As print strategy, we can consider all the main process parameters that are typically defined before each print. The most relevant are layer height, strand dimensions, number of outer shells, and layer time. The layer time is defined as the time required to complete a single layer, i.e., the time taken by the nozzle to deposit the molten material in the same X - Y coordinates of two subsequent layers. Other parameters, such as nozzle diameter, printing speed, and screw rotation, do not directly influence the print thermal behavior since they are tailored accordingly to meet the desired strategy.

Generally speaking, small strands, thin walls, and a large cross-sectional area promote the strand cooling rate. If the strand cools below a specific critical temperature before the subsequent layer has been deposited, no bond formation develops in the strands interface limiting the layer adhesion. As a result, the layer time and therefore the maximum printable part, a distinctive feature of large format additive manufacturing, are temperature restricted and differ from one material to another.

The running setup does not feature any cooling or heating device to manipulate the thermal behavior of the printed material; the cooling rate of the part is solely related to natural cooling dynamics.

2.2.2 Process Window. The process window is defined in terms of deposition temperature. The deposition temperature, T_d , is the temperature of the receiving substrate when the new molten material is deposited on it by the nozzle.

As defined, the process window is characterized by an upper and a lower limit. Higher deposition temperatures affect processability, while lower temperatures influence adhesion between layers.

The upper limit in terms of deposition temperature can be set as the temperature beyond which the process can no longer be defined under stable conditions and sagging and buckling of the printed part may occur. Indeed, the deposited layers do not have the chance to cool down fast enough to guarantee the minimum structural stiffness to withstand the weight of the printed layers. Considering the material flows typically involved in SEAM, such a scenario mainly occurs when relatively small-scale parts with thick walls are printed.

On the other hand, the opposite situation may arise when particularly large parts having a rather long layer time are printed. However, from the printing point of view, there are no actual drawbacks to using low deposition temperatures. Depositing the molten material on a cold layer does not enable proper bond formation and results in poor layer adhesion.

Compared to other applications, in tool manufacturing the mechanical properties and surface finish after milling play a significant role in the product quality. Based on the experience gained through machining printed parts, the lower temperature limit was established as a compromise between a feasible process window, machinability, and mechanical properties and it is defined as the minimum deposition temperature that guarantees at least 80% of the maximum recorded mechanical properties obtained with the optimal printing parameters.

It is therefore crucial to identify both minimum and maximum deposition temperatures to be able to develop a controlled and effective printing process. Differential scanning calorimetry (DSC) analysis provides a preliminary understanding of the thermal behavior of the material and an indicative process window. For the semicrystalline material under analysis, carbon fiber reinforced PA6, the theoretical maximum temperature at which the material can withstand the load of additional layers being deposited over it is the melting temperature. Instead, for optimal bond formation between layers, the lower limit of the process window must be at least equal to the onset of the crystallization. It should be underlined that the mentioned values strongly depend on the heating and cooling rate undergone by the material during the printing process (Ref 25, 39, 40).

To establish the optimal process window and evaluate the mechanical properties in longitudinal and transversal directions, it was necessary to study and develop a test method that meets four requirements:

- The geometry shall be easy to print, scale, and replicate.
- Mechanical testing specimens must be obtained in both X and Z directions.
- Between test prints, only one parameter at a time can be varied.
- The test should produce useful data for industrial practice.

2.2.3 Printing Parameters. For this purpose, a set of single-wall boxes were printed; the prints were designed to differ from each other exclusively in terms of layer time and, as a result, deposition temperature (Fig. 6).

The boxes were printed with a single 4-mm-wide and 1-mm-thick strand produced by a $\text{Ø}3 \times 10$ -mm cylindrical nozzle. The boxes' side dimensions varied between 200 and 1500 mm, while a minimum of 250 layers was printed to accommodate mechanical specimens up to 150 mm in length. To cover a wider range of scenarios and investigate their influence on mechanical properties, the boxes were designed and printed considering two different printing speeds and pressures. The low speed setup was set to 3000 mm/min while a higher speed of 10,000 mm/min, was selected.

The perimeter of the boxes was dimensioned to match the desired layer time. For this study, a total of 21 boxes were printed, 12 of them using the low speed setup and 9 with the high speed setup.

Higher printing speed requires an increased flow rate to achieve the same strand dimension. To vary the mass flow, the screw rotation needs to be adjusted accordingly. The extruder was fine-tuned for both setups to obtain a consistent strand width ranging between 4 and 4.5 mm. Low speed setup

required a screw rotation of 18 rpm, 30 rpm was used for high speed setup.

For a summary of all the printing parameters used in both low and high speed/pressure setups, refer to Table 1.

2.3 Sampling

2.3.1 Temperature. The machine can monitor the extrusion temperature using a temperature probe in contact with the molten polymer. The temperature sensor is placed inside the tip of the extruder and measures the actual printing temperature. Temperature data logging is managed directly by the machine.

The deposition temperature, i.e., the layer temperature on which the molten material is deposited, was recorded using a welded tip K -type thermocouple together with an Easylog data logger produced by Lascar Electronics (Wiltshire, UK). Moreover, an infrared thermographic camera (FLIR E6-Wilsonville, Oregon, USA) was calibrated and used to monitor the temperature distribution on the printed part surface (Fig. 7). The deposition temperature builds up as the number of deposited layers increases, eventually reaching a steady value after about 20 layers. Therefore, the top and bottom 50 mm of every box were removed and discarded. The temperature was measured at different heights throughout the printed part and only the layer temperature at equilibrium is reported.

2.3.2 Pressure. A pressure sensor is integrated inside the print head a few millimeters above the nozzle to record the extruding pressure. Starting from the 20th layer to the end of the print, the pressure was measured for different boxes. Pressure data logging is managed directly by the printing machine.

The pressure is produced by the resistance provided by the nozzle constriction in letting the molten material flow through (Ref 41). Since higher screw rotations result in higher flow rates, the back pressure at the nozzle raises when the extruder speed increases. At 18 rpm the pressure ranges between 13.6 and 14.6 bar, while at 30 rpm it settles between 21.3 and 25.4 bar corresponding to a pressure difference of approximately 50% between low and high speed setups. Therefore, from now on, a high or low setup will be used to express printing parameters in terms of both speed and pressure.

The pressure at the nozzle as a function of the deposition temperature, for low and high setups, is reported in Fig. 8.

For both printing setups, the extruding pressure tends to decrease as the deposition temperature raises showing the lowest values at 190-200 °C. For the same print setup, the pressure reduction at higher deposition temperature can be exclusively associated with the lower back pressure provided by the underlying layer on the molten material escaping the nozzle. According to the dynamic mechanical thermal analysis in Fig. 4, the polymer, as temperatures exceed 180 °C, reveals a fast drop in storage modulus and, simultaneously, an increase in viscous response. The same tendency can be also identified in the strand morphology. Low deposition temperature specimens printed using high speed setup show a U-shaped distorted strand as a consequence of the higher pressure and substrate stiffness; high temperatures and low speed setup, on the other hand, led to un-deformed homogenous edges. The differences in morphology generated by the two setups at different

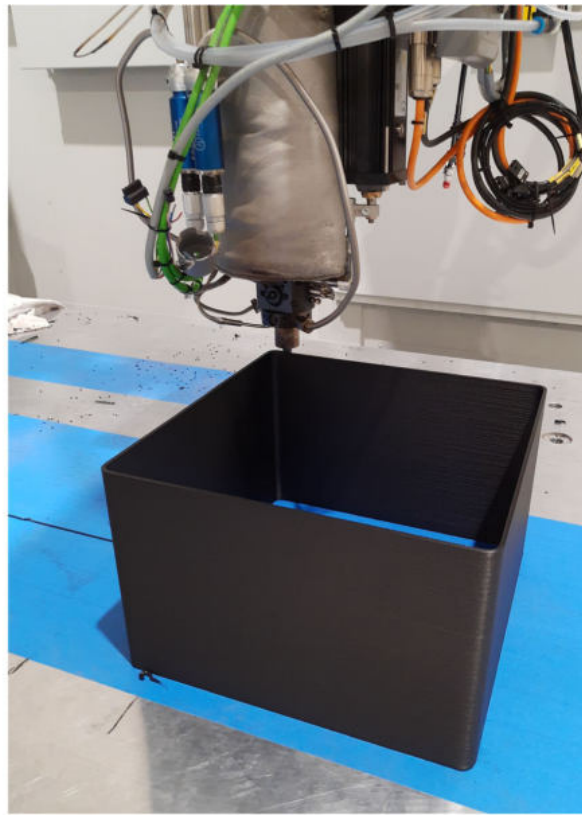
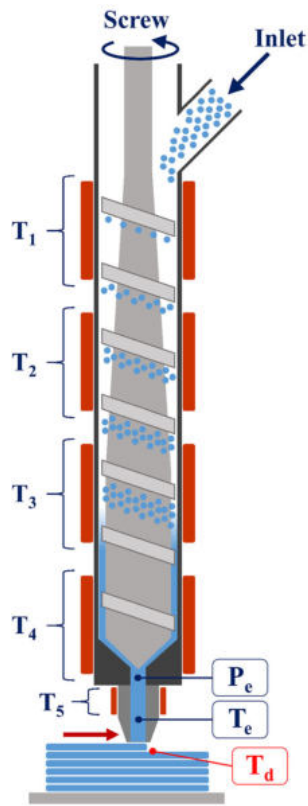


Fig. 6 On the left, depiction of CMS screw extrusion additive manufacturing unit. On the right, 3D printing test setup; a 450×450 mm single shell box during printing

Table 1 Overview and summary of 3D printing parameters in low and high speed setup

Parameters	Unit	Low speed setup	High speed setup
Strand width (W)	mm	4-4.5	
Strand thickness/layer height (H)	mm	1	
Nozzle diameter (D_n)	mm	3	
Printing speed	mm/min	3000	10,000
Extruder rotation	rpm	18	30
Volumetric flow rate (V_f)	cm ³ /min	12.1	40.4
Mass flow rate	kg/h	0.95	3.17
Extrusion pressure (P_e)	bar	13.6-14.6	21.3-25.4
Deposition temperature range (T_d)	°C	80-200	90-190
Zone 1- T_1	°C	255	
Zone 2- T_2	°C	265	
Zone 3- T_3	°C	270	
Zone 4- T_4	°C	280	
Zone 5- T_5 (Nozzle)	°C	280	
Extrusion temperature (T_e)	°C	281	281
Number of printed boxes	...	12	9

deposition temperatures can be seen from the samples' cross-sectional image in Fig. 19 in "Appendix A".

2.4 Samples Preparation

The mechanical properties and layer adhesion were investigated as a function of the deposition temperature. Testing specimens were machined out from the box walls (Fig. 9). For each box, a minimum of six samples per batch were obtained. To keep the sample surface as printed, no machining was

performed on the side of the specimens. Low setup boxes were tested in both longitudinal and transversal directions, and high setup samples were only produced in Z direction.

After the first testing session, an extra box was later printed at high speed setup using the established optimal deposition temperature (150 °C). To achieve the best possible results, the samples were fully machined to remove the rounded side of the strands and obtained a perfectly flat surface.

As-printed un-machined samples were only evaluated under uniaxial tensile loading while fully machined samples were

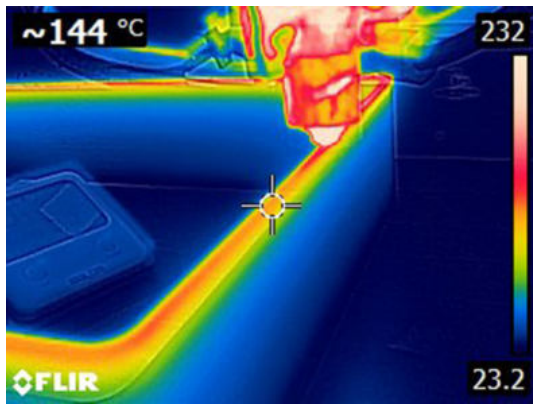


Fig. 7 Temperature distribution on the box during printing. The image was taken using an infrared thermographic camera

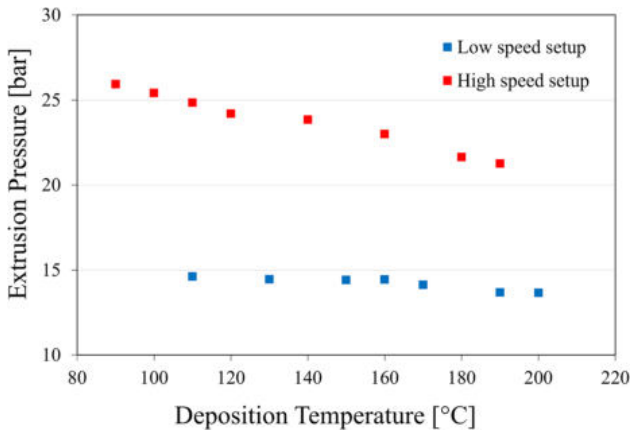


Fig. 8 Low and high setup extrusion pressures as function of the deposition temperature. Pressure decreases with deposition temperature

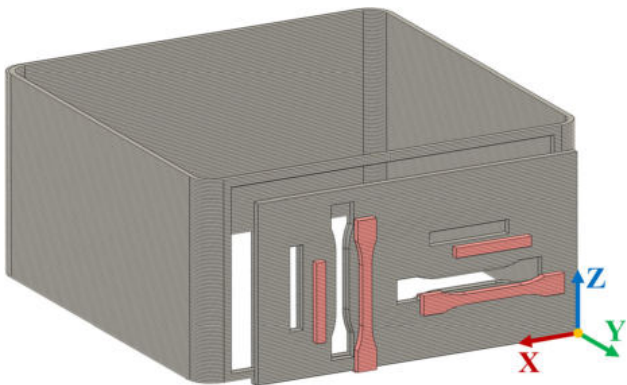


Fig. 9 Longitudinal (X) and transversal (Z) oriented dog bone and flexural samples machined from printed box walls

tested under both tensile and flexural conditions. Before each test, all the samples were previously dried at 60 °C for 24 h under vacuum using a Vacutherm vacuum laboratory oven

produced by Thermo Fisher Scientific (Waltham, Massachusetts, US).

2.5 Testing Techniques

2.5.1 Density Measurement. Pellets and printed part density was measured by buoyancy method according to the standard ASTM D792-13 in both ethanol and water. The results on the printed material match the apparent density determined by measuring the weight and volume of specifically machined samples (Ref 38).

2.5.2 Differential Scanning Calorimetry (DSC). Differential scanning calorimetry was performed on granules and printed parts on a sample mass of about 15 mg using a Mettler DSC 30 calorimeter under a nitrogen flow. The test was run according to the ASTM D3418-21 procedure (Ref 42):

- First heating from 20 to 300 °C at a rate of 10 °C/min
- Cooling from 300 to 20 °C at a rate of -10 °C/min
- Second heating from 20 to 300 °C at a rate of 10 °C/min

During the second heating, the material shows a glass transition temperature of 67 °C; the onset melting temperature and melting temperature peak are, respectively, 209 and 222 °C. In cooling, at a rate of 10 °C/min, the crystallization peak is located between 194 and 184 °C (Fig. 10).

The degree of crystallinity of the samples was calculated according to the equation given in Eq 1:

$$X_c[\%] = \frac{\Delta H_m + \Delta H_c}{\Delta H_m^0 \cdot f} \cdot 100 \quad (\text{Eq 1})$$

where ΔH_m is the integral of the melting peak, ΔH_c is the post-crystallization exothermic enthalpy, f is the PA6 matrix content, and $\Delta H_m^0 = 190$ J/g is the literature melting enthalpy of fully crystalline PA6 (Ref 43).

2.5.3 Tensile Test. Machined printed samples were tested according to the standard UNI EN ISO 527 (Ref 44). Considering the box wall dimensions and thickness, type 1B samples were selected. The gauge length of these dumbbell specimens is 50 mm, with a width of 10 mm and a thickness of 4 mm. For each test batch, a minimum of six specimens were evaluated. Uniaxial tensile tests were performed at room temperature using an Instron 5969 (Instron-Norwood, Massachusetts, USA) electromechanical testing machine equipped with a 50 kN load cell for the longitudinal sample and a 10 kN load cell for transversal ones. Fracture properties were evaluated with a crosshead speed of 10 mm/min while, for the elastic modulus a crosshead speed of 1 mm/min was used. The secant modulus of elasticity was determined between 0.05 and 0.25% strain using an electrical extensometer (Instron model 2620-601) with a 25 mm gauge length.

The transversal properties were evaluated considering the actual contact area between layers, which is equivalent to the sample thickness minus the process-induced peaks/valleys height. The considered strand width is marked using a red dashed line in the cross-sectional image reported in Fig. 19; no noticeable association was observed between effective strand contact width and deposition temperature. In fully machined

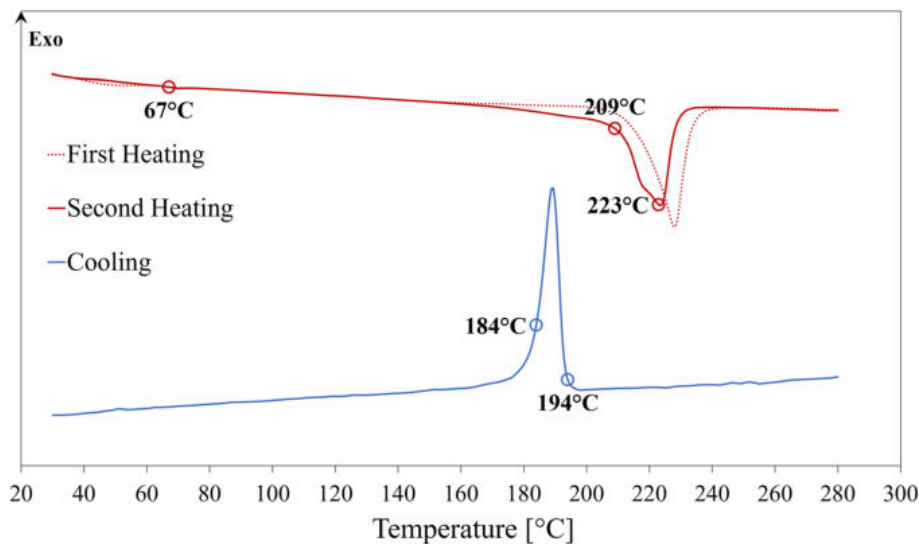


Fig. 10 DSC thermograms and characteristic temperatures of a 40% carbon fiber reinforced polyamide. First heating (dotted red line); cooling (blue line) and second heating (solid red line) were performed at 10 °C/min (Color figure online)

samples, the interlayer contact area matches the sample thickness.

2.5.4 Three Point Bending Test. Flexural testing was conducted according to the standard ASTM D790 (Ref 45). The specimens have a length of 80 mm, a width of 10 mm, and a thickness of 4 mm. The test was performed using an Instron 5969 electromechanical testing machine at a crosshead rate of 2 mm/min. A 50 kN load cell recorded the compressive load on a 64 mm span length. For each test batch, a minimum of six specimens were evaluated.

2.5.5 Dynamic Mechanical Thermal Analysis (DMTA). The viscoelastic properties of the material were studied under dual-cantilever mode by dynamic mechanical thermal analysis using a TA Instruments Q800 DMA (TA Instruments LLC, New Castle, Delaware, USA).

Longitudinal and transversal 3D printed samples were machined to the final dimension of 60 × 10 × 3 mm and, according to ASTM D5418-15, a span length of 35 mm was adopted (Ref 46). Storage (elastic) modulus, loss (viscous) modulus, and $\tan \delta$ were analyzed from 25 to 200 °C at a constant heating rate of 3 °C/min and applying strain of 0.03% at 1 Hz.

2.5.6 Rheological Analysis. Flow properties of the polymer melt were analyzed using a Discovery HR-2 parallel plate rheometer (TA Instruments LLC, New Castle, Delaware, USA). Dynamic shear rheology was performed according to ASTM D4440-15 (Ref 47). 25 mm diameter plate geometry and a gap of 1 mm were selected. Shear viscosity was analyzed by a ramp flow test between 10^{-3} and 10 s^{-1} at 240, 260, and 280 °C. The semicrystalline nature and high fiber content of the polymer lead to rapid viscosity growth when approaching the melting temperature, preventing a reliable measurement by rotational rheology below 240 °C.

2.5.7 Laser Flash Analysis (LFA). The thermal conductivity in *X* and *Z* directions was derived from the thermal diffusivity measured by Laser Flash Analysis using a NETZSCH LFA 467 HyperFlash (NETZSCH Group, Selb,

Germany) according to ASTM E1461-13 (Ref 48). Oriented 12.7 × 2.5 mm cylindrical samples were machined out of a printed plate; a certified Pyroceram 9606 sample was taken as a reference material.

2.5.8 Melt Flow Testing. The melt flow index was assessed in the temperature range going from the extrusion temperature of 280 °C down to 230 °C. According to the standard ASTM D1238-20, an LMI 4002 Melt Indexer produced by Dynisco (Dynisco, Franklin, Massachusetts, USA) was equipped with a 5 kg load, and an extrusion time of 60 s was selected (Ref 49).

2.5.9 Dilatometry. The thermal coefficients of expansion (CTE) in *X* and *Z* directions were measured on a DIL L75 PT Horizontal dilatometer (Linseis Messgeraete GmbH, Selb, Germany). The test was conducted on cylindrical samples with a diameter of 5 mm and a length of 20 mm between 25 and 100 °C using a heating rate of 3.00 °C/min and by applying a constant load of 250 mN according to the standard ASTM E228-17 (Ref 50).

2.5.10 Microscopy. Fiber orientation within the 3D printed strand was investigated by using a Carl Zeiss AG Supra 40 field emission scanning electron microscope (FES-EM) at an acceleration voltage of 6 kV.

The cross section and the fracture surface images of the test specimens were investigated at a 20X magnification using an optical stereomicroscope (Nikon SMZ25-Tokyo, Japan).

3. Results

3.1 Processing Window

The test is designed to identify the upper and lower limits of the printing process window in terms of the deposition temperature of the material laid when the nozzle is extruding the melt above it.

The maximum feasible deposition temperature, at which the printed layers start to collapse, can be easily established by monitoring the printing process itself and can be related to the crystallization onset in fast cooling measured by DSC. For deposition temperatures above 180 °C, the laid material starts to deform and sags under its own weight especially in the case of sloping walls and overhangs.

According to the literature, for a typical 3D printing process cooling rate, the initial crystallization temperature can drop from 194 to 166 °C (Ref 51). Since the substrate layer is close to the crystallization temperature, the material cooling does not occur quickly. As can be seen from the cross-sectional images in Fig. 11 and 19, 190 °C samples show a smooth and rounded strand edge. During new material deposition, the receiving layer was not fully solidified and therefore had the time to rearrange its shape to minimize the free surface area. For larger and more complex prints, such deposition temperatures may already lead to the failure of the printing process.

With good approximation, the maximum deposition temperature can be estimated in the range of the crystallization temperature onset and it sets the upper limit of the process window.

DSC analysis did not exhibit any significant influence of deposition temperature on crystallinity. The average crys-

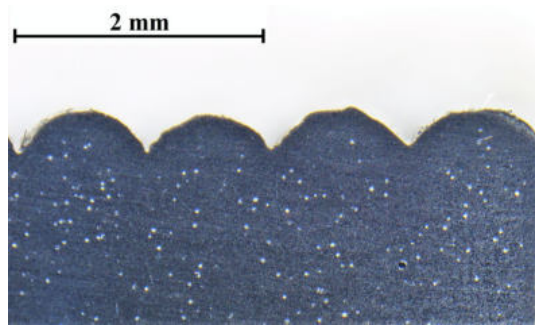
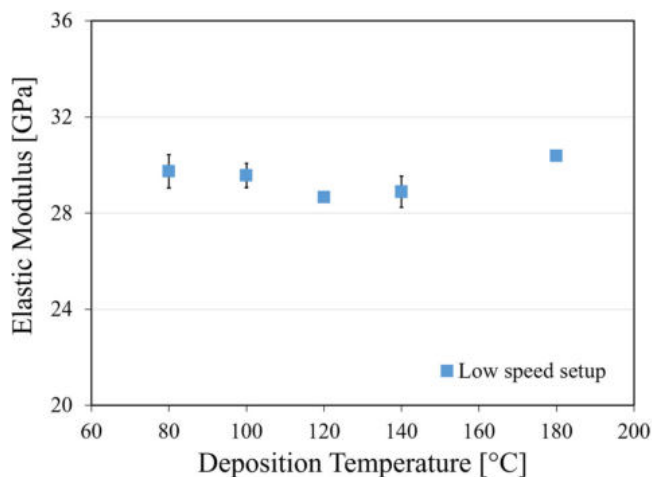


Fig. 11 Neck formation by diffusivity between layers in 190 °C deposition temperature samples



tallinity degree was measured equal to 28.4%, ranging from 27.4 to 30.9%.

The boxes printed with deposition temperatures below 100 °C exhibited fragile behavior during the machining operations. During milling, the poor adhesion between layers led to a brittle failure and crack of multiple samples showing the lower process limit for part machinability. Mechanical tests were carried out to determine the minimum deposition temperature that could guarantee at least 80% of the best-performing setup.

3.2 Mechanical Properties

3.2.1 Longitudinal Samples (X). Tensile test samples in the longitudinal direction show an elastic modulus between 28.7 and 30.4 GPa (Fig. 12). The highest modulus was obtained with the highest deposition temperatures. The same result was provided by the fracture tests, with stress at break ranging between 212.5 and 230.5 MPa showing a slight increase with temperature. Tensile properties in the longitudinal direction were not significantly affected by lower deposition temperature showing a minimum value equal to 92% of the best-performing sample. The impact of the layer adhesion does not appreciably influence the material properties when subjected to stresses aligned to the printing direction promoting layer separation. For that reason, high setup samples were not produced to be tested in longitudinal direction.

3.2.2 Transversal Samples (Z). All transversal specimens, whose performance is closely related to the adhesion between layers, showed an increasing elastic modulus as the deposition temperature increased. The sample printed using low speed setup shows values between 3.5 and 4.7 GPa with the maximum value being measured at 190 °C. The specimens produced with high speed/pressure setup behave similarly but exhibit slightly higher Young's modulus ranging from 3.80 to 5.06 GPa.

A more significant temperature dependence was observed in the ultimate stress at break (Fig. 13).

The minimum value of 5.2 MPa was measured on 80 °C samples while 150 °C ones performed the best showing 42.8 MPa; deposition temperatures above 160 °C and below

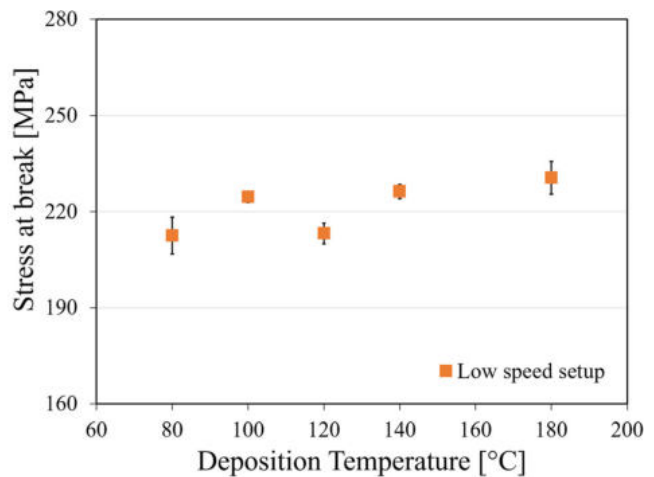


Fig. 12 Tensile elastic modulus and stress at break of X oriented samples as function of the deposition temperature

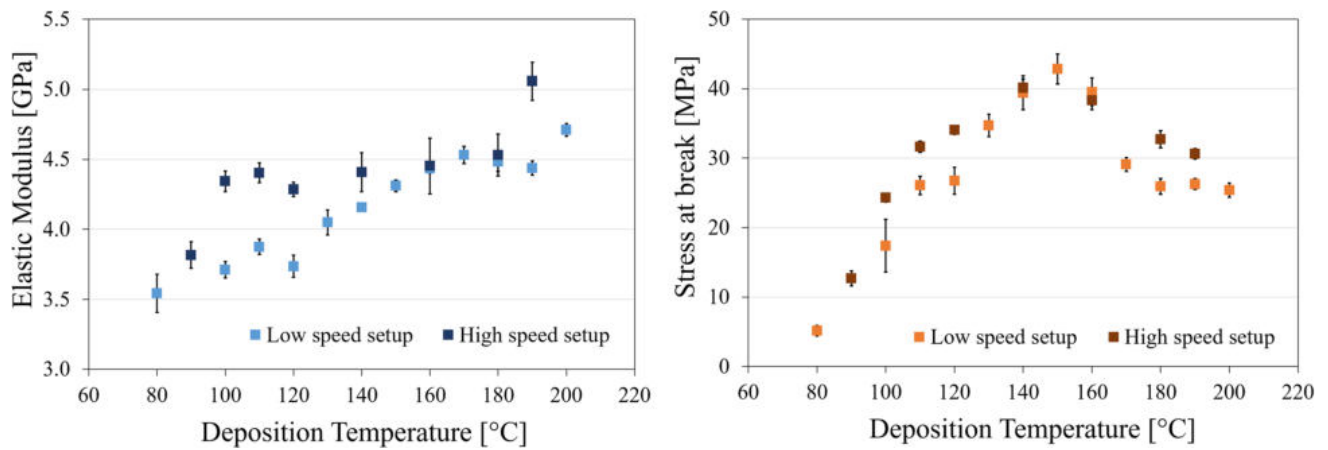


Fig. 13 Tensile elastic modulus and stress at break of Z oriented samples as function of the deposition temperature for high and low speed setup

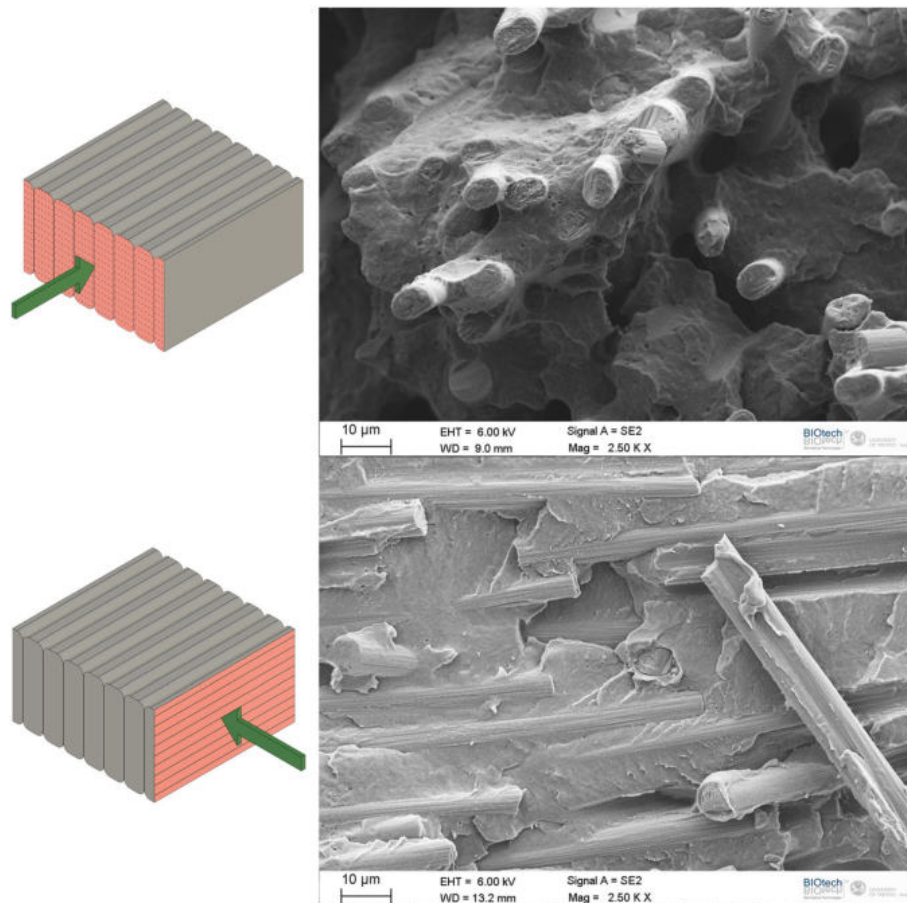


Fig. 14 Scanning electron microscopy (SEM) images of sample fracture surface and graphical representation of the view: X sample on the top and Z oriented sample on the bottom image

130 °C led to a drastic decay in performance. Samples produced with high speed-pressure show a similar trend but more consistent values ranging from 12.47 to 40.1 MPa; the highest value was found at 140 °C. Deposition temperatures below 120 °C do not guarantee at least 80% of the maximum recorded value.

As already mentioned, the influence of extrusion pressure was tested only in the transversal direction where printing parameters seem to have a relevant impact on layer adhesion and mechanical properties in comparison with X direction. The extruder pressure at the nozzle recorded during tests for the two different setups is reported in Fig. 8.

Compared to lower speed, high speed setup translated in higher extrusion pressure and general improvement of material performance, especially for the stress at break between 120 and 180 °C. Tensile strength is less influenced by deposition temperature and exhibits a significantly smaller standard deviation. Moving from the ideal printing temperature, the specimens showed a drop in performance. In the case of high-pressure printing, the loss is not as severe as it is shown by low speed setup samples.

Low deposition temperature transversal specimens exhibited a fragile behavior during testing, resulting in fast crack propagation and low strain at break. The maximum elongation was achieved using the high-pressure setup in combination with a deposition temperature between 140 and 160 °C. Strain at break behaved much like the ultimate tensile stress.

3.3 Machined Samples

Fully machined samples, printed using a deposition temperature of 150 °C, were assessed under flexural and tensile loading and the results are reported in Fig. 3. Longitudinal tensile samples exceed the values of injection-molded samples in both elastic modulus and stress at break reaching 32.7 GPa and 249.92 MPa, respectively. Transversal samples manifest only 15% of the values of *X* samples showing 5.03 GPa and 39.03 MPa; strain at break was measured to be as low as 1.51%, while 3.32% was reached for longitudinal specimens.

Flexural tests on longitudinal samples indicated an elastic modulus of 22.96 GPa and a strength of 347.49 MPa. On the other hand, transversal samples under flexure only reached a modulus of 4.74 GPa and a strength of 71.98 MPa, showing approximately 21% of the values of *X*-oriented samples.

3.4 Fracture Analysis and Strand Shape

The fracture surfaces of *X* and *Z* oriented samples were analyzed by scanning electron microscopy and the micrographs are reported in Fig. 14. The failure was generated under bending by using a couple of pliers after cooling the sample in liquid nitrogen.

The surfaces of both longitudinal and transversal samples show highly oriented fibers, directed along the print direction. In addition to the images, the strongly aligned arrangement of the fibers can also be detected by the highly anisotropic behavior shown in dilatometry where CTE in the transverse direction *Z* is approximately 20 times higher than along the print direction (*X*) (Fig. 5).

Via ImageJ software (Ref 52), the average fiber diameter was estimated to be approximately 7 μm while the length ranges from 120 to 220 μm. The fracture images in Fig. 14 show a surprisingly packed material with no major porosity site. The rupture can induce failure of the polymer–fiber interface resulting in pullout and formation of circular voids inside the matrix as well as fiber breakage. Partially or fully exposed fibers exhibit evident traces of matrix patches, which is a sign of effective impregnation and a strong interface between fiber and polymer.

An optical microscope was used to inspect the sample cross section and fracture surface. The interested reader can refer to Fig. 19 for all microscope images of 80-90, 100, 160, and 190 °C *Z* direction samples printed with low and high speed setups. Fully machined longitudinal and transversal samples are also reported.

Especially for *Z*-oriented samples, observing the specimen's fracture surface may help explain the mechanical behavior and

degree of bonding. Different printing setups and deposition temperatures produced different fracture surfaces. If the interface fails before the material can be completely loaded, an interlayer adhesion fracture surface is shown. Depending on whether the material or the interface fails, a different ratio of inter- and intra-layer failure is produced.

Crack propagation is driven by the least resistance direction toward which the adjacent material fails more easily. Intralayer material breakage exhibits an opaque texture and tends to develop on multiple fractural planes. Interlayer adhesion failure, on the other hand, spreads preferentially within the adhesion plane showing the smooth finish of the underlying substrate.

Higher deposition temperature mainly resulted in material failure within the strand while, as deposition temperature is lowered, more interlayer adhesion failure is shown. Intermediate temperatures generate a combination of the two types of failure. Deposition temperatures above 150 °C, including fully machined optimized transversal samples, have exhibited a 100% interlayer fracture surface. Regardless of the setup, 80 and 90 °C low-temperature specimens failed entirely for faulty adhesion of layers interface. Predictably, the specimens exhibiting mostly material failure were able to withstand higher stress at break. High speed setup printed samples have shown less interlayer failure compared to low speed setup.

In addition, it can be noted that, the strands' cross-sectional shape changes according to the deposition temperature and extrusion pressure. Higher deposition temperature and lower pressure generate more homogenous and rounded strand edges. Such morphology can be related to a not fully solidified receiving layer and a lower pushing action produced by the extruded material escaping the nozzle. Lowering the deposition temperature and increasing the extruder pressure deform the strand generating an upwards-faced concave shape. The solidified substrate layer impedes the flow of molten material increasing extrusion pressures and producing a deformed strand.

3.5 Annealing

In addition to the mechanical characterization of the printed part, the effects of post-print heat treatment were assessed. The annealing process aims to enhance the performance of the printed part by increasing the adhesion between layers. The thermal treatment was conceived to be performed on large format 3D printed parts using traditional industrial equipment.

Annealing is a heat treatment process commonly used to improve the mechanical properties, heat, and chemical resistance of polymers (Ref 53, 54). In some applications, manufacturers include annealing stress relief to meet dimensional requirements (Ref 55). Annealing of semicrystalline polymers is generally performed between the glass transition temperature (T_g) and the melting temperature (T_m). Considering the promising results available in the literature regarding the annealing of PA6 3D printed parts (Ref 56, 57), it was then decided to explore the effectiveness of the treatment in improving adhesion between layers and mechanical properties in the *Z*-direction.

To highlight the benefits of the annealing treatment, low-temperature samples were selected as a reference. A hexagonal one-shelled box was printed using a high speed setup and a deposition temperature of 90 °C.

Six box walls were obtained; five of them were annealed for 8 h in static air at different constant temperatures: 120, 140,

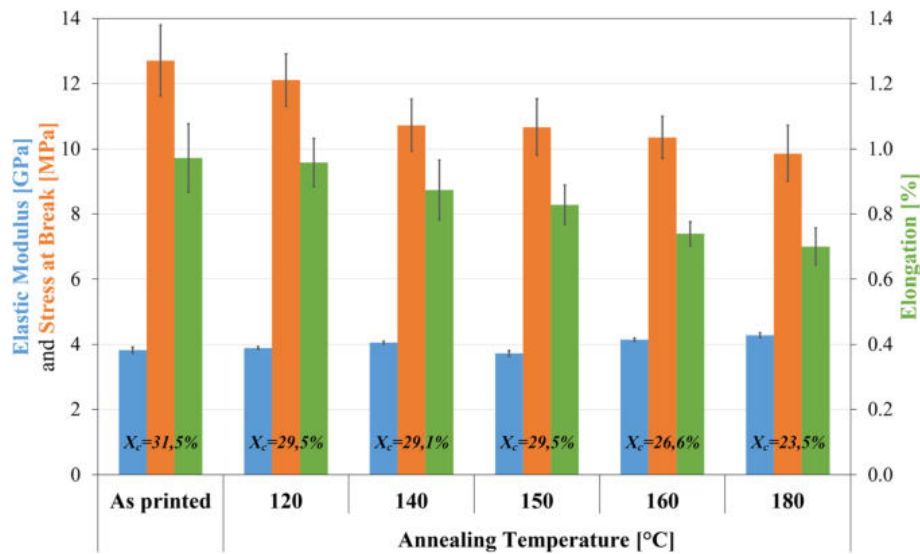


Fig. 15 Mechanical properties and degree of crystallinity X_c of Z annealed samples as function of the heat treatment temperature

150, 160, and 180 °C in a Vacutherm laboratory oven by Thermo Fisher Scientific. The walls were left to cool down to 60 °C before removing them from the oven. For each wall, eight tensile dumbbell test specimens were machined.

Considering the shape, weight, and tolerances of the typically printed part, 180 °C was taken as the maximum feasible heat treatment temperature to guarantee the dimensional stability of the final part.

The tensile samples were machined out from the five treated walls and tested. The results, in terms of maximum tensile stress, elastic modulus, and elongation at break, are reported in Fig. 15. The degree of crystallinity was also evaluated for all the samples and is shown in the same graph.

The annealing procedure brought a slight, though not significant, increase in elastic modulus. On the other hand, compared to the untreated specimens, there was a significant decrease in elongation, stress at break, and crystallinity. The worst performances were recorded at the treatment temperature of 180 °C, with a drop in tensile strength from 12.7 to 9.8 MPa. It can be deduced that no significant benefit to the mechanical properties of printed parts was induced by the proposed heat treatment.

4. Discussion

A screw extrusion additive manufactured component will typically exhibit anisotropic mechanical properties. The material extruded from the nozzle consists of a heavily aligned polymer and fiber composite strand. As a result, along the printing direction, both the elastic modulus and the stress at break are roughly five times higher than in the transverse direction. The performance of a tensile test specimen is associated with its weakest section. For a longitudinal specimen, where the strands are aligned with the loading axis, the cross section is almost uniform along the whole gauge length of the specimen. The layer interface, lying parallel to the load, is not directly subjected to an opening action. For this reason, the inter-strand degree of adhesion does not significantly affect the performance of the specimens in the X -direction. By contrast,

transverse tensile specimens present multiple process-induced discontinuities transversally located to the loading direction; the most crucial is the layer-layer bond interfaces. In 3D printed samples, the fracture typically originates from the valleys between two strands' edges and develops along the least resistance path. Limited layer adhesion facilitates fracture growth within the strands interface leading to a rapid interlayer failure. When bond formation between layers is better developed, the interface produces a stronger resistance to fracture that moves within the solid strand. The ultimate tensile stresses reached by an intralayer fracture generally exceed the ones measured for an interlayer fracture (Ref 58, 59). The test samples produced with low deposition temperature exhibited mostly interlayer failure. Higher deposition temperatures, on the other hand, promoted bond formation showing mainly material failure within the layer.

As already mentioned, bond formation is a temperature-driven phenomenon strictly related to the macromolecule diffusion between layers. The molecular motion of polymer chains is associated with low material viscosity. By rotational rheometer measurement, the polymer exhibits a shear-thinning behavior as the melt viscosity decreases with increase in shear rate. A cross model fit was used to estimate flow behavior inside the screw extrusion additive manufacturing process shear rate window, between 20 and 500 s^{-1} . Flow viscosity curves as a function of shear rate at 240, 260, and 280 °C are shown in Fig. 16.

The processing data, which are reported in Table 1, were used to estimate the shear rate and thus viscosity for low and high print setups. The shear rate $\dot{\gamma}$ was evaluated according to Rabinowitsch's corrected cylindrical flow channel equation (Eq 2) for shear-thinning materials (Ref 60).

$$\dot{\gamma} [s^{-1}] = \frac{3n + 1}{4n} \cdot \frac{32 \cdot \text{Volume flow rate}}{\pi \cdot \text{Nozzle } \phi^3} \quad (\text{Eq 2})$$

where n is the power index obtained from the viscosity fitting at 280 °C in the SEAM range.

The low speed setup, producing a limited volume flow rate, does not induce the same shear rate as the high speed setup which shows roughly 50% higher values. The estimated flow

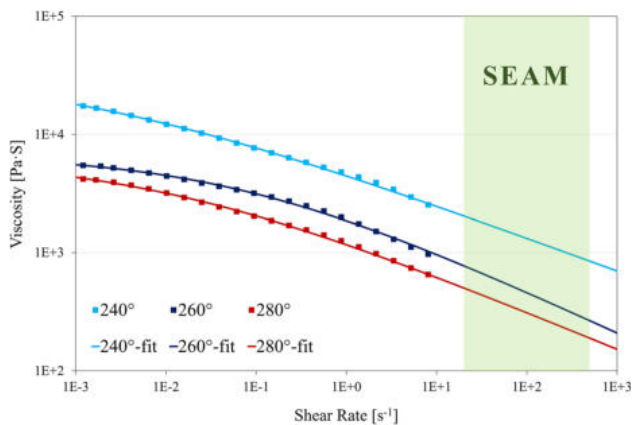


Fig. 16 Viscosity as function of shear rate measured by parallel plate rheometer at 240, 260, and 280 °C between 0.01 and 100 s⁻¹. Typical shear rates of the extrusion process are highlighted in green

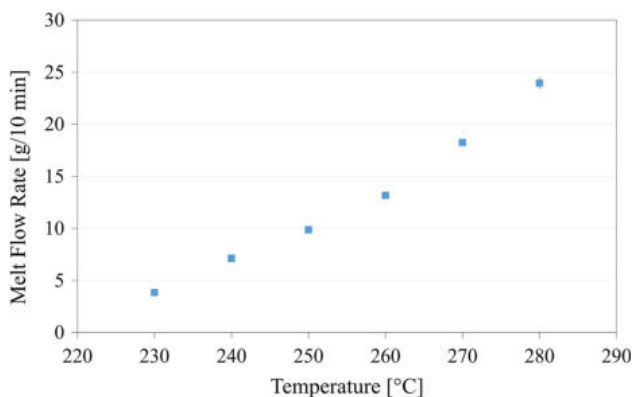


Fig. 17 Effect of processing temperature on the melt flow rate of 40% carbon fiber reinforced polyamide 6

viscosities at 280 °C result equal to 325 Pa s for the low speed setup and 225 Pa s for the high speed setup.

High speed parameters produce higher pressure and lower viscosity compared to low speed setup, ensuring quicker surface wetting, void filling, and overall better interfacial contact between layers. As result, it was observed that higher extrusion pressure positively influenced the transversal mechanical properties of the printed samples. The increased pressure and lower melt viscosity generate a progressive distortion of the deposited strand producing a concave geometry and thus larger weld lengths (Ref 30, 61). The superior layer adhesion of high speed and pressure setup is further evidenced by the higher intra/interlayer failure ratio at the fracture surface compared to low speed and pressure setup.

Besides showing overall better mechanical properties, in terms of both ultimate tensile strength and elastic modulus, it was noticed less fluctuation, more consistent performance, and less temperature influence, especially in the low side of the deposition temperature range.

Although greater pressures ensure faster intimate contact and thus longer time for diffusion and healing, bond formation is primarily driven by the material temperature at the interface. As illustrated by flow viscosity curves, the cooling from the extrusion temperature of 280 °C to a lower temperature of 240 °C results in a viscosity gain of nearly 300%. Another

evidence of the sudden drop of the melt flowability approaching the crystallization temperature can be provided by MFR measurements as well. In Fig. 17, the melt flow rate as a function of different extrusion temperatures is plotted. For temperatures below 230 °C, material motion is severely reduced compared to the values measured at 280 °C.

For semicrystalline polymers, the minimum temperature that allows molecular diffusion and interfacial bond formation is the onset of the melting peak. Under the hypothesis of constant heat capacity, constant thermal diffusivity, and perfect contact between strands interface, Plummer suggested calculating the average interfacial temperature using the equation given in Eq 3 (Ref 62):

$$T_{i,a}[\text{°C}] = \frac{T_d + T_e}{2} \quad (\text{Eq 3})$$

where $T_{i,a}$ is the average interfacial temperature, T_d is the deposition temperature, and T_e is the extrusion temperature.

According to the equation, considering a melting onset of 209 °C, a temperature of at least 140 °C is required to develop interlayer bond formation. Indeed, the best results were found above 140 °C, which might be interpreted as the lower limit of the narrow processing window.

Although the effectiveness of an overheated 3D printing process has already been proved, the extrusion temperature was optimized and kept constant at 280 °C (Ref 29). Boosting the extrusion temperature is usually the easiest way to provide a temperature rise at the interface regardless of the deposition temperature; such a solution, however, might produce unstable deposition and inconsistent quality of the part, therefore, it is not explored in this paper.

The temperature at the interface is equally affected by the deposition temperature, here assumed as the main process variable. A warmer substrate not only guarantees a higher average interface temperature and, consequently, a longer diffusion time before crystallization takes place, but also a lower viscosity which further promotes weld formation between layers. An intimate voidless contact between the lower strand and the deposited molten material increases diffusion area resulting in less interfacial porosity and generally better bonding. By definition, the bond strength between two layers is a function of the interfacial contact area, which can be enhanced by a higher flowability and wetting of the molten polymer on the lower strand. In extrusion-related processes, the ability of the polymer melt to flow under pressure can be assessed from the melt flow rate data. As shown in Fig. 11, specimens printed using high deposition temperatures feature a smoother strand edge and a principle of diffusion neck between strands.

As result, the best performances were achieved at higher deposition temperatures. In the 80-200 °C temperature range, transversal elastic modulus increases almost linearly with deposition temperature. Higher pressures generally resulted in improved adhesion, especially at the edges of the deposition temperature window. The stress at break reveals the major performance variation among the different deposition temperatures; the best-performing samples, the ones between 140 and 160 °C, doubled the results of low deposition temperature samples. According to the Z samples tensile test, this could be defined as the optimal process window. On the other hand, the minimum deposition temperature to guarantee a sufficient layer adhesion, assuming to perform at least 80% of the best sample, was set equal to 120 °C.

By measuring the polymer characteristic temperatures in cooling and heating, DSC analysis is an effective tool to obtain useful indications in defining the upper and lower process limits. The maximum deposition temperature is the temperature above which the structural solidity of the printed workpiece and a controlled deposition process is no longer guaranteed. Based on experimental print trials, the maximum deposition temperature was set equal to 180 °C; such value can be related to the onset of the crystallization peak that ranges between 194 and 166 °C depending on the cooling rate. As can be seen from the DMTA curves in Fig. 4, approaching 180 °C, the material shows a more viscous and less elastic behavior. The drop in storage modulus is clear evidence of reduced stiffness and increased molecular motion of polymer chains. For both setups, the extrusion pressure decreases as the deposition temperature increases, which is indicative of the fact that a warmer substrate provides less resistance to the melt exiting the nozzle. On a morphological level, the deformation of the deposited strand, which can be associated with a more constricted flow, occurs as the temperature of the underlying layer decreases and is more severe in specimens printed with high-pressure setups and lower viscosity.

Contrary to expectations, the highest tensile stress at break was not recorded at the highest deposition temperature. Indeed, due to the pressure influence on layer adhesion, it can be assumed that the best performance stemmed from a combined effect of deposition temperature and pressure; above 160 °C, the gain in interfacial temperature does not compensate for the undesirable pressure drop associated with higher temperatures.

In comparison with the as-printed specimens characterized by a process-induced morphology, at the same condition of deposition temperatures and pressure, fully machined specimens exhibited a significant improvement in elastic modulus yet a similar tensile strength. Such a result can be related to the different influences of sample morphologies on elastic modulus and stress at break.

From a process standpoint, in typical industrial practice, the deposition temperature is controlled by properly managing the layer time. Starting from the CAD model and the required tool specifications, the wall thickness, strand size, and printing strategy are then established. By feeding those parameters into a database, the optimal layer time to guarantee a deposition temperature between 140 and 160 °C is estimated. The database is material-specific and is generated and expanded

by continuous print process data collection. Longer layer times correspond to lower deposition temperatures, and vice versa shorter layer times will lead to higher deposition temperatures. According to the path length, the printing speed is tuned to match the target layer time. Depending on the technical specifications of the printer, particularly small or large components might preclude a perfect optimization of the deposition temperature; nevertheless, it is important to maintain the deposition temperature in the 120-180 °C range. The process window is assured by monitoring real-time in-process temperatures of the deposited material by an infrared camera, an optical pyrometer, or a contact thermocouple.

Layer time is the guiding parameter in print path programming as it restricts the maximum print size, a peculiar feature of the LFAM process. Different substrate preheating solutions based on infrared laser and lamp have been explored to extend the layer time; although the topic is beyond the scope of this work, it is one of the most attractive fields of improvement for industrial practice (Ref 63-65).

Deposition temperature is also promoted by larger strand dimensions which are characterized by a lower specific surface and thus lower cooling rate. A thicker strand enables longer layer time while reducing the extrusion pressure at the nozzle, which, as discussed earlier, must be also considered. The equation given in Eq 4 can determine the required pressure to extrude a strand of known dimension and setup assuming a rectangular flow channel (Ref 30).

$$P[\text{Pa}] = \frac{12 \cdot \eta \cdot \text{Volume flow rate} \cdot L}{W \cdot H^3} \quad (\text{Eq 4})$$

where L is the flow length in the nozzle terminal section and is equal to 10 mm, W is the strand width and H is the layer height; the values are reported in Table 1. The evolution of the extrusion pressure as a function of print speed and strand height for the two setups is shown in Fig. 18.

In both print conditions, assuming constant strand width, a thinner layer requires higher extrusion pressures. For a given nozzle and strand size, a higher flow rate leads to greater flow resistance and lower viscosity. Lowering the layer height while increasing the printing speed can ensure higher deposition pressure and wetting; polymer melt is pushed into intimate contact and promotes a stronger layer adhesion (Ref 61). On the other hand, an exaggerated layer height, despite leading to less

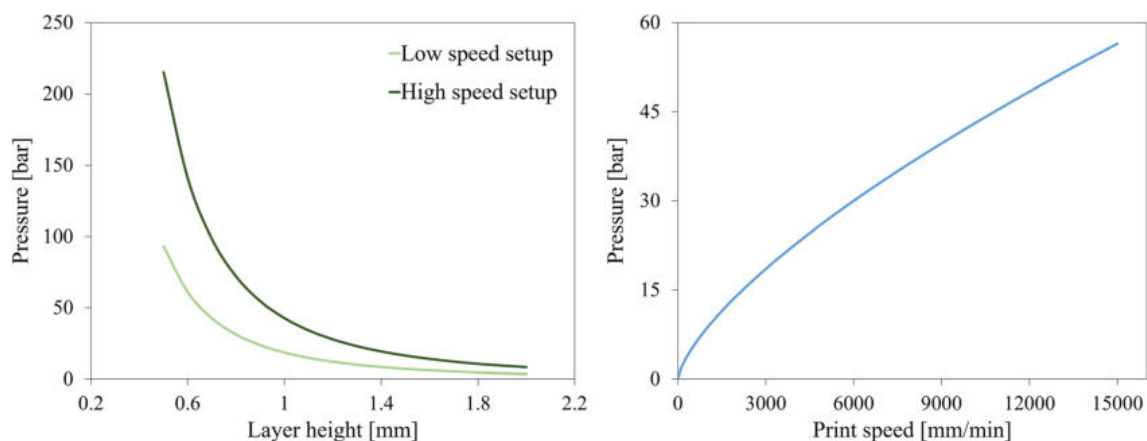


Fig. 18 On the left, extrusion pressure as function of layer height for low (3000 mm/min) and high speed setup (10,000 mm/min). On the right, extrusion pressure as function of print speed

heat loss and better adhesion temperature, drastically reduces the back pressure. The influence of strand dimension on thermo-mechanical properties and anisotropy certainly needs further investigation.

It should be clarified that the print test experiment performed in the study was designed to reproduce the worst adhesion conditions by using a single-strand wall. Multi-strand printing strategy mitigates the performance decay at low deposition temperatures and generally leads to a better overall tool performance. Indeed, by printing more than one strand side by side, the rapid cooling and part temperature unevenness are reduced while increasing contact area and strand mechanical interlocking. Moreover, as already pointed out, tooling is not as demanding as structural applications are in terms of mechanical properties; tool handling and machining, in most cases, turn out to be the most critical phases of the entire production process.

5. Summary and Conclusions

The process analyzed in this research is large format additive manufacturing by screw extrusion for the production of industrial tools. In this paper, the influence of deposition temperature and extrusion pressure on the mechanical properties of the printed component was investigated. The target material is a 40% carbon fiber reinforced polyamide 6. Aiming at optimizing the material mechanical properties and surface quality required by industry standards; the results were used to determine the optimal process window and tool thermo-mechanical qualification.

The following conclusions for process optimization can be deduced:

- Higher deposition temperature and pressure combined with lower viscosity promote faster surface wetting, void filling, and overall better interfacial contact between layer and thus greater diffusion and bond formation. Working at higher pressure ensures more consistent result and generally better performance in comparison with lower pressure.
- The printed material showed highly anisotropic mechanical and thermal behavior associated with the directionality of the high carbon fiber content. Differentiated CTEs for *X*-*Y* plane and *Z* build direction shall be assumed for tool dimensional compensation and to minimize distortion during print arrangement.
- The mechanical properties in the transverse direction (*Z*) depend on both deposition temperature and extrusion pressure and find an optimal compromise in the 140-160 °C range. The best results are obtained at 150 °C using the high-pressure-speed setup. Transversal ultimate tensile stress and elastic modulus of machined samples reach roughly a fifth of the longitudinal values. On the other hand, tensile and flexural performance along the print direction (*X*) direction are essentially unaffected by layer adhesion and deposition temperature exceeding the material manufacturer's datasheet by approximately 10%.
- Based on test results, the process window has been defined between 120 and 180 °C. Temperature below 120 °C induces a rapid drop in performance while deposition temperature above 180 °C cannot guarantee a

stable and consistent printing process. Deposition temperatures below 100 °C produce an extremely brittle printed material, compromising the machinability of the component.

The annealing heat treatment did not provide any beneficial result on the mechanical properties of the print workpiece, confirming that no molecular diffusion and therefore interlayer bond formation develops below the melting onset. While unlikely to be implemented on large printed tools, additional testing at higher temperatures might reveal potential improvement in layer adhesion.

The material has proven to be an excellent solution for machining tool, assembly jig and caliber, as it exhibits high stiffness and dimensional stability up to 50 °C; hardness and post-machining surface finish are essential features for master models and lamination molds. Long-term dimensional stability is definitely a concern when comes to tools; in the way parts were produced and preserved, PA6 hygroscopy did not appear to be as critical as expected (Ref 32).

Additionally, the aim of this article is to address the main process-related challenges experienced during the optimization and fine-tuning of an innovative manufacturing process that involves a new material; it is intended to outline an analytical approach that could be replicated on other industrially attractive materials, like ABS, PC, and PEI, to complete the tooling application scenario.

Acknowledgments

This research project is financially supported by the company CMS Spa (Zogno, Italy).

Funding

Open access funding provided by Università degli Studi di Trento within the CRUI-CARE Agreement.

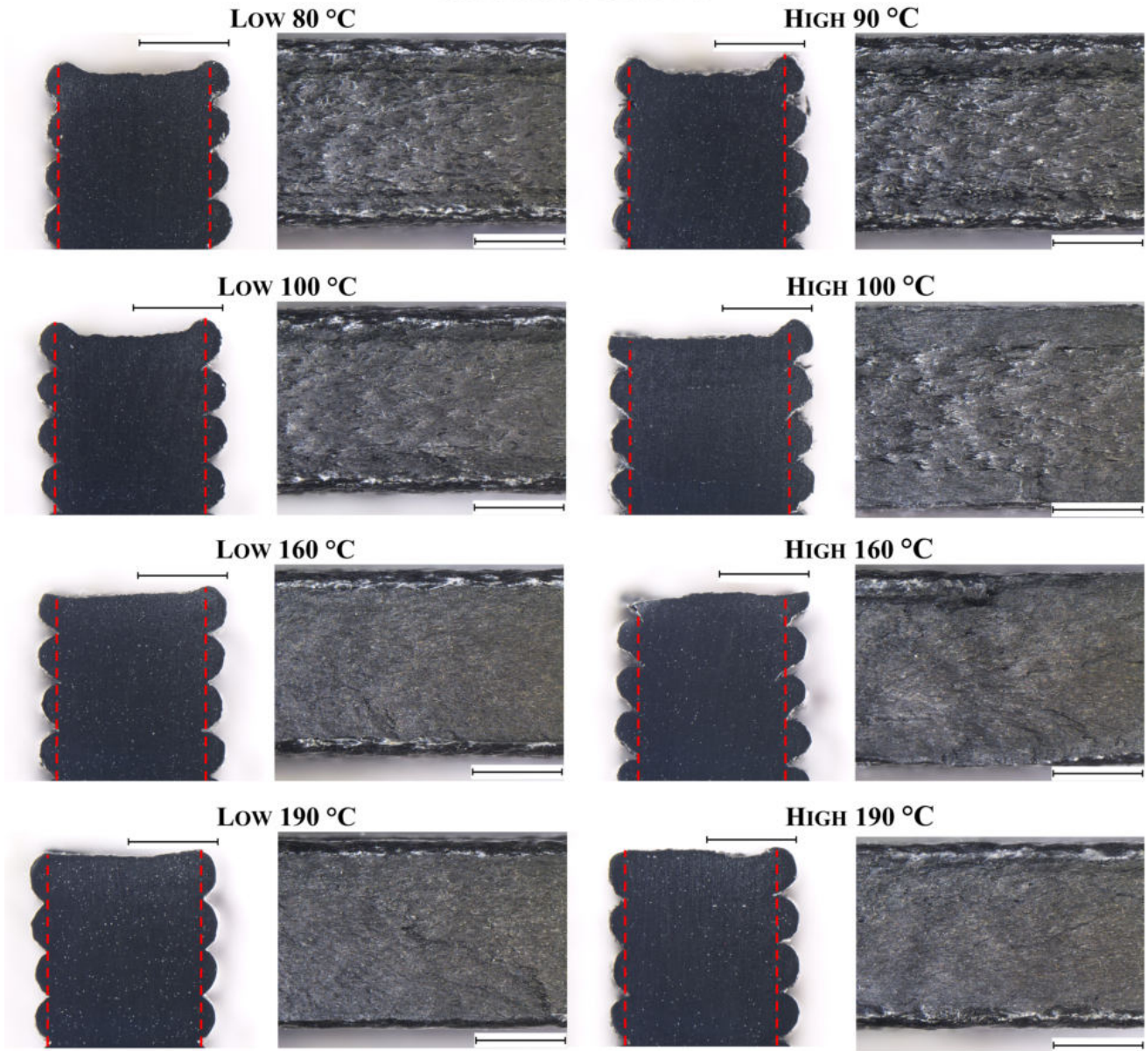
Open Access

This article is licensed under a Creative Commons Attribution 4.0 International License, which permits use, sharing, adaptation, distribution and reproduction in any medium or format, as long as you give appropriate credit to the original author(s) and the source, provide a link to the Creative Commons licence, and indicate if changes were made. The images or other third party material in this article are included in the article's Creative Commons licence, unless indicated otherwise in a credit line to the material. If material is not included in the article's Creative Commons licence and your intended use is not permitted by statutory regulation or exceeds the permitted use, you will need to obtain permission directly from the copyright holder. To view a copy of this licence, visit <http://creativecommons.org/licenses/by/4.0/>.

Appendix A

See Fig. 19.

AS PRINTED Z SAMPLES



FULLY MACHINED SAMPLES

Z - HIGH SPEED 150 °C

X - HIGH SPEED 150 °C

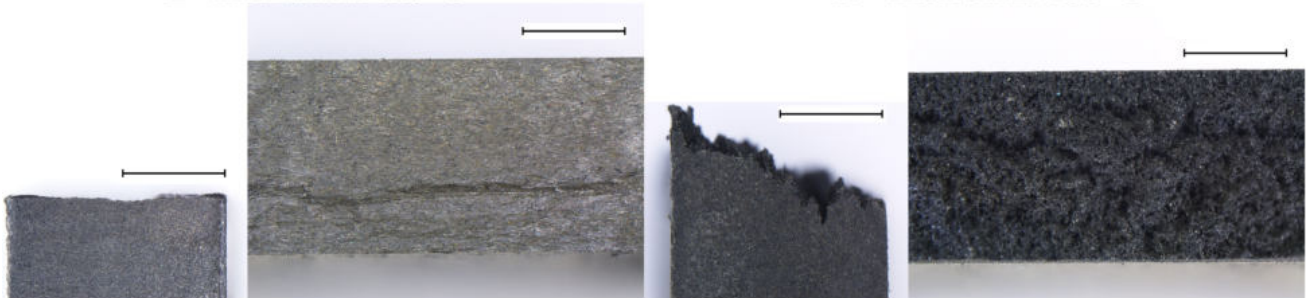


Fig. 19 Cross section and fracture surface images of as-printed Z samples at different deposition temperature for low and high speed setup (top); the strands contact width is marked using red dashed line. Cross section and fracture surface images of fully machines X and Z samples (bottom). Scale bar is 2 mm in all images

References

1. Additive Manufacturing—General Principles—Fundamentals and Vocabulary, 52900-21, ISO/ASTM (2022). <https://doi.org/10.1520/f3177-21>
2. M. Attaran, The Rise of 3-D Printing: The Advantages of Additive Manufacturing Over Traditional Manufacturing, *Bus. Horiz.*, 2017, **60**(5), p 677–688. <https://doi.org/10.1016/j.bushor.2017.05.011>
3. Technical Specifications—CMS Kreator, CMS S.p.A. <http://scmgroupp.com/it/cmsadvancedmaterials/products/>. Accessed 5 July 2022
4. Technical Specifications—AM Flexbot, CEAD B.V. <http://ceadgroup.com/solutions/robot-based-solutions/>. Accessed 5 July 2022
5. Technical Specifications—LSAM, Thermwood Corporation. http://thermwood.com/lsam_home.htm. Accessed 5 July 2022
6. X. Li, J. He, Z. Hu, X. Ye, and S. Wang, High Strength Carbon-Fiber Reinforced Polyamide 6 Composites Additively Manufactured by Screw-Based Extrusion, *Compos. Sci. Technol.*, 2022, **229**, p 109707. <https://doi.org/10.1016/j.compscitech.2022.109707>
7. P. Malnati, *Hybrid, Large-Format Additive Tooling: Lighter, Faster, Less Costly Molds for Big Parts*. Composite World. Accessed 20 November 2020
8. S. Black, *3D Printing Moves into Tooling Components*. Composite World. Accessed 15 June 2015
9. S. Dul, L. Fambri, and A. Pegoretti, High-Performance Polyamide/Carbon Fiber Composites for Fused Filament Fabrication: Mechanical and Functional Performances, *J. Mater. Eng. Perform.*, 2021, **30**, p 5066–5085. <https://doi.org/10.1007/s11665-021-05635-1>
10. L.J. Love, V. Kunc, O. Rios, C.E. Duty, A.M. Elliott, B.K. Post, R.J. Smith, and C.A. Blue, The Importance of Carbon Fiber to Polymer Additive Manufacturing, *J. Mater. Res.*, 2014, **29**, p 1893–1898. <https://doi.org/10.1557/jmr.2014.212>
11. J. Li and X. Cheng, The Effect of Carbon Fiber Content on the Friction and Wear Properties of Carbon Fiber Reinforced Polyimide Composites, *J. Appl. Polym. Sci.*, 2008, **2008**(107), p 1737–1743. <https://doi.org/10.1002/app.27273>
12. K. Sertoglu, *Ingersoll and BELL 3d Printed a 22-Foot-Long Rotor Blade Mold in 75 hours*. 3D Printing Industry. Accessed 1 April 2021
13. S. Davies, *Airtech Advanced Materials Group Makes Dahltram Tooling Resins Available for Thermwood LSAM 3D printing*. TCT Magazine. Accessed 22 September 2021
14. H. Mason, *Collaborative Boeing-Led Project Validates Large-Scale Composite AM Tooling*. Composite World. Accessed 18 November 2021
15. A. Das, C.A. Chatham, J.J. Fallon, C.E. Zawaski, and E.L. Gilmer, Current Understanding and Challenges in High Temperature Additive Manufacturing of Engineering Thermoplastic Polymers, *Addit. Manuf.*, 2020, **34**, p 101218. <https://doi.org/10.1016/j.addma.2020.101218>
16. B.G. Compton, B.K. Post, C.E. Duty, L. Love, and V. Kunc, Thermal Analysis of Additive Manufacturing of Large-Scale Thermoplastic Polymer Composites, *Addit. Manuf.*, 2017, **17**, p 77–86. <https://doi.org/10.1016/j.addma.2017.07.006>
17. B. Brenken, E. Barocio, A. Favaloro, V. Kunc, and R.B. Pipes, Fused Filament Fabrication of Fiber-Reinforced Polymers: A Review, *Addit. Manuf.*, 2018, **21**, p 1–16. <https://doi.org/10.1016/j.addma.2018.01.002>
18. N.M. Cococetta, D. Pearl, M.P. Jahan, and J. Ma, Investigating Surface Finish, Burr Formation, and Tool Wear During Machining of 3D Printed Carbon Fiber Reinforced Polymer Composite, *J. Manuf. Process.*, 2020, **56**, p 1304–1316. <https://doi.org/10.1016/j.jmapro.2020.04.025>
19. Y. Zhao, Y. Chen, and Y. Zhou, Novel Mechanical Models of Tensile Strength and Elastic Property of FDM AM PLA Materials: Experimental and Theoretical Analyses, *Mater. Des.*, 2019 <https://doi.org/10.1016/j.matdes.2019.108089>
20. P. Consul, A. Chaplin, N. Tagscherer, S. Zaremba, and K. Drechsler, Interlaminar Strength in Large-Scale Additive Manufacturing of Slow Crystallizing Polyaryletherketone Carbon Composites, *Polym. Int.*, 2021, **70**, p 1099–1108. <https://doi.org/10.1002/pi.6168>
21. P.G. De Gennes, Reptation of a Polymer Chain in the Presence of Fixed Obstacles, *J. Chem. Phys.*, 1971, **55**(2), p 572–579. <https://doi.org/10.1063/1.1675789>
22. R.P. Wool and K.M. Oconnor, A Theory of Crack Healing in Polymers, *J. Appl. Phys.*, 1981, **52**(10), p 5953–5963. <https://doi.org/10.1063/1.328526>
23. J. Bartolai, T.W. Simpson, and R. Xie, Predicting Strength of Additively Manufactured Thermoplastic Polymer Parts Produced Using Material Extrusion, *Prototyp. J.*, 2018, **24**(2), p 321–332. <https://doi.org/10.1108/RPJ-02-2017-0026>
24. M.A. Yardimci and S. Guceri, Conceptual Framework for the Thermal Process Modelling of Fused Deposition, *Rapid Prototyp. J.*, 1996, **2**(2), p 26–30. <https://doi.org/10.1108/13552549610128206>
25. C.M. Stokes-Griffin and P. Compston, Investigation of Sub-melt Temperature Bonding of carbon-Fiber/PEEK in an automated Laser Tape Placement Process, *Compos. A Appl. Sci. Manuf.*, 2016, **84**, p 17–25. <https://doi.org/10.1016/j.compositesa.2015.12.019>
26. Q. Sun, G.M. Rizvi, C.T. Bellehumeur, and P. Gu, Effect of Processing Conditions on the Bonding Quality of FDM Polymer Filaments, *Rapid Prototyp. J.*, 2008, **14**(2), p 72–80. <https://doi.org/10.1108/13552540810862028>
27. B.N. Turner, R. Strong, and S.A. Gold, A Review of Melt Extrusion Additive Manufacturing Processes: I. Process Design and Modeling, *Rapid Prototyp. J.*, 2014, **20**(3), p 192–204. <https://doi.org/10.1108/RPJ-01-2013-0012>
28. Y.-Q. Xue, T.A. Tervoort, and P.J. Lemstra, Welding Behavior of Semicrystalline Polymers. 1. The Effect of Nonequilibrium Chain Conformations on Autoadhesion of UHMWPE, *Macromolecules*, 1998, **31**(9), p 3075–3080. <https://doi.org/10.1021/ma970544u>
29. T.Q. Tran, C. Canturri, X. Deng, C.L. Tham, and F.L. Ng, Enhanced Tensile Strength of Acrylonitrile Butadiene Styrene Composite Specimens Fabricated by Overheat Fused Filament Fabrication Printing, *Compos. B Eng.*, 2022 <https://doi.org/10.1016/j.compositesb.2022.109783>
30. T.J. Coogan and D.O. Kazmer, Bond and Part Strength in Fused Deposition Modeling, *Rapid Prototyp. J.*, 2017, **23**(2), p 414–422. <https://doi.org/10.1108/RPJ-03-2016-0050>
31. V. Kishore, X. Chen, C. Ajinjeru, and A.A. Hassen, Additive Manufacturing of High Performance Semicrystalline Thermoplastics and Their Composites, in *26th Annual International Solid Freeform Fabrication Symposium*, Austin, USA (2016)
32. G. Chabaud, M. Castro, C. Denoual, and A. Le Duigou, Hygro-mechanical Properties of 3D Printed Continuous Carbon and Glass Fibre Reinforced Polyamide Composite for Outdoor Structural Applications, *Addit. Manuf.*, 2019, **26**, p 94–105. <https://doi.org/10.1016/j.addma.2019.01.005>
33. C. Duty, C. Ajinjeru, V. Kishore, and B. Compton, What Makes a Material Printable? A Viscoelastic Model for Extrusion-Based 3D Printing of Polymers, *J. Manuf. Process.*, 2018, **35**, p 526–537. <https://doi.org/10.1016/j.jmapro.2018.08.008>
34. J.L.C. Quintana, L. Slattery, J. Pinkham, J. Keaton, R.A. Lopez-Anido, and K. Sharp, Effects of Fiber Orientation on the Coefficient of Thermal Expansion of Fiber-Filled Polymer Systems in Large Format Polymer Extrusion-Based Additive Manufacturing, *Materials*, 2022, **15**, p 2764. <https://doi.org/10.3390/ma15082764>
35. Technical Datasheet—AKROMID® B3 ICF 40 black (5020), Akroplastic GmbH. <http://akro-plastic.com>. Accessed 5 July 2022
36. N. Van De Werken, H. Tekinalp, P. Khanbolouki, S. Ozcan, A. Williams, and M. Tehrani, Additively Manufactured Carbon Fiber-Reinforced Composites: State of the Art and Perspective, *Addit. Manuf.*, 2020, **31**, p 100962. <https://doi.org/10.1016/j.addma.2019.10.0962>
37. Plastics and Ebonite—Determination of Indentation Hardness by Means of a Durometer (Shore hardness), 868, ISO (2003)
38. Standard Test Methods for Density and Specific Gravity (Relative Density) of Plastics by Displacement, D 792-20, ASTM (2020). <https://doi.org/10.1520/d0792-20>
39. F. Yang and R. Pitchumani, Healing of Thermoplastic Polymers at an Interface Under Nonisothermal Conditions, *Macromolecules*, 2002, **35**(8), p 3213–3224. <https://doi.org/10.1021/ma010858o>
40. D. Grewell and A. Benatar, Welding of Plastics: Fundamentals and New Developments, *Int. Polym. Process.*, 2007, **22**(1), p 43–60. <https://doi.org/10.3139/217.0051>
41. T.J. Coogan and D.O. Kazmer, Modeling of Interlayer Contact and Contact Pressure During Fused Filament Fabrication, *J. Rheol.*, 2019, **63**, p 655–672. <https://doi.org/10.1122/1.5093033>
42. Standard Test Method for Transition Temperatures and Enthalpies of Fusion and Crystallization of Polymers by Differential Scanning Calorimetry, D 3418-21, ASTM (2021). <https://doi.org/10.1520/d3418-21>

43. R.H. Mehta, Physical constants of various polyamides, *Polymers Handbook*. J. Brandrup, E.H. Immergut, E.A. Grulke Ed., Wiley, Hoboken, 1999, p V/126
44. Plastics—Determination of Tensile Properties—Part 2: Test Conditions for Moulding and Extrusion Plastics, 527-2, ISO (2012)
45. Standard Test Methods for Flexural Properties of Unreinforced and Reinforced Plastics and Electrical Insulating Materials, D 790-17, ASTM (2017). <https://doi.org/10.1520/d0790-17>
46. Standard Test Method for Plastics: Dynamic Mechanical Properties: In Flexure (Dual Cantilever Beam), D5418-15, ASTM (2016). <https://doi.org/10.1520/d5418-15>
47. Standard Test Method for Plastics: Dynamic Mechanical Properties Melt Rheology,” D4440-15, ASTM (2015). <https://doi.org/10.1520/D4440-15>
48. Standard Test Method for Thermal Diffusivity by the Flash Method,” E1461—13, ASTM (2022). <https://doi.org/10.1520/E1461-13R22>
49. Standard Test Method for Melt Flow Rates of Thermoplastics by Extrusion Plastometer, D1238-20, ASTM (2020). <https://doi.org/10.1520/d1238-20>
50. Standard Test Method for Linear Thermal Expansion of Solid Materials with a Push-Rod Dilatometer, E228-17, ASTM (2017). <https://doi.org/10.1520/e0228-17>
51. N. Tagscherer, P. Consul, I.L. Kottenstedde, H. Latiri, S. Zaremba, and K. Drechsler, Investigation of Nonisothermal Fusion Bonding for Extrusion Additive Manufacturing of Large Structural Parts, *Polym. Compos.*, 2021, **42**, p 5209–5222. <https://doi.org/10.1002/pc.26216>
52. W.S. Rasband, ImageJ (Version 1.53s), U. S. National Institutes of Health. <https://imagej.nih.gov/ij/>. Accessed 19 May 2022
53. J. Butt and R. Bhaskar, Investigating the Effects of Annealing on the Mechanical Properties of FFF-Printed Thermoplastics, *J. Manuf. Mater. Process.*, 2020, **4**(2), p 38. <https://doi.org/10.3390/jmm4020038>
54. Y. Srithep, P. Nealey, and L.-S. Turng, Effects of Annealing Time and Temperature on the Crystallinity and Heat Resistance Behavior of Injection-Molded Poly(lactic acid), *Polym. Eng. Sci.*, 2013, **53**, p 580–588. <https://doi.org/10.1002/pen.23304>
55. Y. Zhang and S.K. Moon, The Effect of Annealing on Additive Manufactured ULTEM™ 9085 Mechanical Properties, *Materials*, 2021, **14**(11), p 2907. <https://doi.org/10.3390/ma14112907>
56. M. Handwerker, J. Wellnitz, H. Marzbani, and U. Tetzlaff, Annealing of Chopped and Continuous Fibre Reinforced Polyamide 6 Produced by Fused Filament Fabrication, *Compos. B. Eng.*, 2021 <https://doi.org/10.1016/j.compositesb.2021.109119>
57. Z. Ali, Y. Yan, H. Mei, L. Cheng, and L. Zhang, Effect of Infill Density, Build Direction and Heat Treatment on the Tensile Mechanical Properties of 3D-Printed Carbon-Fiber Nylon Composites, *Compos. Struct.*, 2023, **304**, p 116370. <https://doi.org/10.1016/j.compstruct.2022.116370>
58. B. Rankouhi, S. Javadpour, F. Delfanian, and T. Letcher, Failure Analysis and Mechanical Characterization of 3D Printed ABS With Respect to Layer Thickness and Orientation, *J. Fail. Anal. Prevent.*, 2016, **16**, p 467–481. <https://doi.org/10.1007/s11668-016-0113-2>
59. A.R. Torrado Perez, D.A. Roberson, and R.B. Wicker, Fracture Surface Analysis of 3D-Printed Tensile Specimens of Novel ABS-Based Materials, *J. Fail. Anal. Prevent.*, 2014, **14**, p 343–353. <https://doi.org/10.1007/s11668-014-9803-9>
60. Y. Son, Determination of Shear Viscosity and Shear Rate from Pressure Drop and Flow Rate Relationship in a rectangular Channel, *J. Polym.*, 2007, **48**(2), p 632–367. <https://doi.org/10.1016/j.polymer.2006.11.048>
61. C.A. Butler, R.L. McCullough, R. Pitchumani, and J.W. Gillespie, An Analysis of Mechanisms Governing Fusion Bonding of Thermoplastic Composites, *J. Thermoplast. Compos. Mater.*, 1998, **11**(4), p 338–363. <https://doi.org/10.1177/089270579801100404>
62. C.J.G. Plummer, P.-E. Bourban, J.-E. Zanetto, G.D. Smith, and J.-A.E. Månson, Nonisothermal Fusion Bonding in Semicrystalline Thermoplastics, *J. Appl. Polym. Sci.*, 2003, **87**, p 1267–1276. <https://doi.org/10.1002/app.11528>
63. V. Kishore, C. Ajinjeru, A. Nycz, B. Post, J. Lindahl, V. Kunc, and C. Duty, Infrared Preheating to Improve Interlayer Strength of Big Area Additive Manufacturing (BAAM) Components, *Addit. Manuf.*, 2017, **14**, p 7–12. <https://doi.org/10.1016/j.addma.2016.11.008>
64. N. Tagscherer, T.A. Osswald, and K. Drechsler, Targeted Temperature Manipulation and Analysis of the Influence on Mechanical Properties in Large-Scale Extrusion Additive Manufacturing, *Appl. Sci.*, 2022, **12**, p 2998. <https://doi.org/10.3390/app12062998>
65. A.K. Ravi, A. Deshpande, and K.H. Hsu, An in-Process Laser Localized Pre-deposition Heating Approach to Inter-layer Bond Strengthening in Extrusion Based Polymer Additive Manufacturing, *J. Manuf. Process.*, 2016, **24**, p 179–185. <https://doi.org/10.1016/j.jma.2016.08.007>

Publisher's Note Springer Nature remains neutral with regard to jurisdictional claims in published maps and institutional affiliations.